Bioverse: Giant Magellan Telescope and Extremely Large Telescope direct imaging and high-resolution spectroscopy assessment—surveying exo-Earth O2 and testing the habitable zone oxygen hypothesis

Hardegree-Ullman, K.K.; Apai, D.; Haffert, S.Y.; Schlecker, M.; Kasper, M.; Kammerer, J.; Wagner, K.

The Astronomical Journal, 169:171 (20pp), 2025 March https://doi.org/10.3847/1538-3881/adb02f

Bioverse: Giant Magellan Telescope and Extremely Large Telescope Direct Imaging and High-resolution Spectroscopy Assessment—Surveying Exo-Earth O_2 and Testing the Habitable Zone Oxygen Hypothesis

Kevin K. Hardegree-Ullman[1,2], Dániel Apai[1,3], Sebastiaan Y. Haffert[1,4], Martin Schlecker[1], Markus Kasper[5], Jens Kammerer[5], and Kevin Wagner[1]
[1] Steward Observatory, The University of Arizona, 933 N. Cherry Ave., Tucson, AZ 85721, USA; kevinkhu@caltech.edu
[2] Caltech/IPAC-NASA Exoplanet Science Institute, 1200 E. California Blvd., MC 100-22, Pasadena, CA 91125, USA
[3] Lunar and Planetary Laboratory, The University of Arizona, 1629 E. University Blvd., Tucson, AZ 85721, USA
[4] Leiden Observatory, Leiden University, PO Box 9513, 2300 RA Leiden, The Netherlands
[5] European Southern Observatory, Karl-Schwarzschild-Straße 2, 85748 Garching bei München, Germany
Received 2024 May 16; revised 2025 January 23; accepted 2025 January 28; published 2025 February 26

Abstract

Biosignature detection in the atmospheres of Earth-like exoplanets is one of the most significant and ambitious goals for astronomy, astrobiology, and humanity. Molecular oxygen is among the strongest indicators of life on Earth, but it will be extremely difficult to detect via transmission spectroscopy. We used the Bioverse statistical framework to assess the ability to probe Earth-like O_2 levels on hypothetical nearby habitable zone exo-Earth candidates (EECs) using direct imaging and high-resolution spectroscopy on the Giant Magellan Telescope (GMT) and the Extremely Large Telescope (ELT). Assuming continued improvement in instruments and data processing, our analysis highlights the best-case scenarios. Earth-like O_2 levels could be probed on up to ∼7 and ∼19 EECs orbiting bright M dwarfs within 20 pc in a hypothetical 10 yr survey on the GMT and ELT, respectively. Four known super-Earth candidates, including Proxima Centauri b, could be probed for O_2 within about 1 week of observations on the ELT and a few months on the GMT. We also assessed the ability of the ELT to test the habitable zone oxygen hypothesis—that habitable zone Earth-sized planets are more likely to have O_2—within a 10 yr survey using Bioverse. Testing this hypothesis requires either ∼one-half of the EECs to have O_2 or ∼one-third if $\eta_\oplus$ is large. A Northern Hemisphere large-aperture telescope, such as the Thirty Meter Telescope, would expand the target star pool by about 25%, reduce the time to probe biosignatures on individual targets, and provide an additional independent check on potential biosignature detections.

Unified Astronomy Thesaurus concepts: Exoplanet systems (484); Exoplanets (498); Exoplanet atmospheres (487); Biosignatures (2018); Astrobiology (74); Habitable zone (696); Habitable planets (695); Astronomical simulations (1857); Bayesian statistics (1900); Parametric hypothesis tests (1904)

1. Introduction

Methods for probing the atmospheres of exoplanets have matured to the point that we are within reach of biosignature detection on rocky worlds. Transmission spectroscopy has become a powerful tool to characterize the atmospheres of planets from the ground (e.g., I. A. G. Snellen et al. 2008, 2010; K. B. Stevenson et al. 2014), and from space with the Hubble Space Telescope (e.g., D. Charbonneau et al. 2002; D. K. Sing et al. 2016; Z. Zhang et al. 2018) and now JWST (e.g., JWST Transiting Exoplanet Community Early Release Science Team et al. 2023; S. E. Moran et al. 2023). In the search for biosignatures via transmission spectroscopy, JWST might prove fruitful in the detection of species such as CH_4, H_2O, and CO_2 (e.g., F. Wunderlich et al. 2019), however, it will not be able to detect O_2 (J. Lustig-Yaeger et al. 2019; F. Wunderlich et al. 2019; D. Pidhorodetska et al. 2020), a major by-product of the biological process of oxygenic photosynthesis on Earth. I. A. G. Snellen et al. (2013), F. Rodler & M. López-Morales (2014), D. B. Serindag & I. A. G. Snellen (2019), M. López-Morales et al. (2019), M. H. Currie et al. (2023), and K. K. Hardegree-Ullman et al. (2023) studied the prospects of detecting O_2 via transmission spectroscopy using upcoming 25–40 m class telescopes such as the Giant Magellan Telescope (GMT; M. Johns et al. 2012), Thirty Meter Telescope (TMT; J. Nelson & G. H. Sanders 2008; G. H. Sanders 2013), and the European Southern Observatory Extremely Large Telescope (ELT; R. Gilmozzi & J. Spyromilio 2007). K. K. Hardegree-Ullman et al. (2023) took into account practical ground-based observing constraints such as transit observability and relative system velocities to mitigate telluric blending. They concluded that even in a very optimistic observing scenario where signals from the GMT, TMT, and ELT and all observable transits could be combined, it will likely take decades to make an O_2 detection on a single transiting habitable zone Earth-sized exoplanet.

This study explores whether direct imaging is more efficient for O_2 surveys. Previous studies suggest it might be possible to detect biosignatures using reflected-light spectroscopy on directly imaged planets (e.g., I. Snellen et al. 2015; C. Lovis et al. 2017). To date, high-contrast imaging has been limited to young, self-luminous gas giants on wide orbits (e.g., G. Chauvin et al. 2004; C. Marois et al. 2008; A. M. Lagrange et al. 2009; B. Macintosh et al. 2015; M. Keppler et al. 2018). This is mainly due to telescope apertures limiting the inner working angle at which a planet is detectable (often similar to the Rayleigh criterion, $\sim 1.22\lambda/D$, where λ is the observing wavelength and

D is the primary mirror diameter) and due to contrast limitations of current high-contrast imaging systems.

1.1. Previous Direct Imaging Studies

There have been numerous studies investigating the potential for a next-generation space telescope (e.g., LUVOIR, HabEx, and LIFE; The LUVOIR Team 2019; B. S. Gaudi et al. 2020; S. P. Quanz et al. 2022) to probe biosignatures in reflected light with direct imaging and low-resolution spectroscopy (e.g., Y. K. Feng et al. 2018; A. Bixel & D. Apai 2021; M. Damiano & R. Hu 2022; B. S. Konrad et al. 2022; T. D. Robinson & A. Salvador 2023; N. Susemiehl et al. 2023). Due to the recommendations brought forth in the Astro2020 Decadal Survey (NASEM 2021), the Habitable Worlds Observatory (HWO) is being developed with the goal to identify and directly image at least 25 potentially habitable worlds using a telescope about the same size as JWST and optimistically launching in the 2040s. In the meantime, the GMT, TMT, and ELT are expected to be operational in the early 2030s. The significantly larger apertures of these telescopes will be able to probe smaller inner working angles and study the habitable zones of nearby M dwarfs, which will be inaccessible to HWO.

Ground-based spectroscopy of biosignatures necessitates the use of high-resolution spectrographs ($R \gtrsim 50{,}000$) to allow separation of Earth's telluric lines from those of the exoplanet atmosphere, assuming sufficient line Doppler shifts to minimize line blending (see, e.g., F. Rodler & M. López-Morales 2014; M. López-Morales et al. 2019, for examples of different resolutions and their effect on line blending). W. B. Sparks & H. C. Ford (2002) proposed combining a coronographic imager with a high spectral resolution integral-field spectrograph for detection and characterization of exoplanets. As I. Snellen et al. (2015) showed, the achievable contrast of a combined high-contrast imaging and high-resolution spectrograph system is the product of the individual system achievable contrasts. For example, if each individual system can reach a contrast of $\sim 10^{-5}$, the combined system could reach contrasts of $\sim 10^{-10}$ (see additional discussion in Section 2.2).

Notable observational developments have been made in this observing technique for measuring the optical albedo of hot Jupiters τ Boötis b (e.g., D. Charbonneau et al. 1999; C. Leigh et al. 2003; F. Rodler & M. López-Morales 2014; H. J. Hoeijmakers et al. 2018) and 51 Pegasi b (J. H. C. Martins et al. 2015). The first tentative detection came from J. H. C. Martins et al. (2015) who took 90 high-resolution spectra of 51 Pegasi b with HARPS over the span of 3 months and used cross-correlation methods to measure a 3.7σ upper limit to the planet-to-star contrast ratio of 6×10^{-5}, corresponding to a relatively high albedo of 0.5. This signal has been both confirmed (E. F. Borra & D. Deschatelets 2018) and disputed (P. Di Marcantonio et al. 2019; G. Scandariato et al. 2021; E. F. Spring et al. 2022). H. J. Hoeijmakers et al. (2018) combined more than 2000 spectra collected over 15 yr from four different facilities to measure a 3σ upper limit to the planet-to-star contrast ratio of 1.5×10^{-5} and a relatively low optical albedo of $\sim$0.12 for τ Boötis b. These studies indicate the potential difficulty of using high-contrast imaging with high-resolution spectroscopy to detect planets in reflected light, but this could be due to the low albedo of hot Jupiters at optical wavelengths (M. Brogi & J. Birkby 2021). Measuring reflected-light signals from terrestrial planets may pose similar problems, but we optimistically continue to build and expand upon the techniques learned from reflected-light studies of hot Jupiters.

I. Snellen et al. (2015) investigated using a high-resolution ($R = 100{,}000$) optical spectrograph in combination with an extreme adaptive optics (AO) system on the ELT to observe a hypothetical 1.5 $R_\oplus$ planet in the habitable zone of Proxima Centauri in reflected light (prior to the discovery of Proxima Centauri b by G. Anglada-Escudé et al. 2016). They concluded that such a planet would be detectable in broadband (0.6–0.9 μm) reflected light in 10 hr of integration time at a signal-to-noise ratio (S/N) of $\sim$10 after cross correlating the hypothetical observed spectrum with a model template spectrum, but they did not explore specific biosignature detection.

Since its discovery, most of the focus on high-contrast imaging and high-resolution reflected-light spectroscopy has been on Proxima Centauri b. This is likely driven by the planet's location within the habitable zone, and a measured minimum mass ($M \sin i$) likely between 1.0 $M_\oplus$ (M. Damasso et al. 2020) and 1.27 $M_\oplus$ (G. Anglada-Escudé et al. 2016). A. Bixel & D. Apai (2017) placed probabilistic mass and radius constraints on Proxima Centauri b of $M = 1.63^{+1.66}_{-0.72}\ M_\oplus$ and $R = 1.07^{+0.38}_{-0.31}\ R_\oplus$, which are consistent with a rocky composition, but there is still a $\sim$10% chance the planet has a significant amount of ice or a volatile envelope. We do not yet have enough information to truly constrain the nature of Proxima Centauri b, so assuming it is Earth-like or an Earth analog is an optimistic assumption.

C. Lovis et al. (2017) proposed upgrades to SPHERE and ESPRESSO on the Very Large Telescope in order to observe Proxima Centauri b with high-resolution reflected-light spectra. They adopted a 3D global climate model atmosphere of Proxima Centauri b from M. Turbet et al. (2016), assumed observations at orbital quadrature, and a spectrograph resolution of 220,000. They concluded a 3.6σ detection of O_2 could be made in about 60 nights of telescope time over the course of 3 yr.

J. Wang et al. (2017) simulated observations in reflected light with low- to high-resolution spectra of Proxima Centauri b (assuming it is an Earth-like planet) and a hypothetical Earth-like habitable zone planet orbiting an M dwarf at 5 pc using a 30 m class telescope in near-infrared bands. They used near-infrared (1–2.5 μm) $R = 1000$–$100{,}000$ Earth-like exoplanet spectra, considering atmospheric chemistry, and using a radiative transfer model from R. Hu et al. (2012a, 2012b, 2013) and R. Hu & S. Seager (2014). For a 100 hr integration time, their simulations yielded S/N > 10 for H_2O, O_2, CO_2, and CH_4, typically when $R > 10{,}000$ and starlight suppression was $>10^{-7}$. These simulations simplistically addressed line blending, assuming the radial velocity of the exoplanet shifts its atmospheric signature by tens of kilometers per second. An updated version of this analysis was provided by H. Zhang et al. (2024), where they simulated direct imaging of 10 nearby rocky planets at $R = 1000$ with HARMONI-like and METIS-like instruments on the ELT in search of biosignatures. They indicated that CO_2, CH_4, and H_2O should be detectable on GJ 887 b and Proxima Centauri b at an S/N > 5 with integration times on the order of <100 hr.

G. A. Hawker & I. R. Parry (2019) focused on the detectability of Earth-like levels of O_2 on Proxima Centauri b with high-resolution spectroscopy and high-contrast imaging

on the ELT using HIRES- and HARMONI-like instruments. They concluded an S/N = 3–5 detection could be obtained in 30–70 hr of integration time. More recently, S. R. Vaughan et al. (2024) simulated observations of Proxima Centauri b using HARMONI on the ELT at its highest resolving power of $R = 17{,}385$. Their simulations indicated an atmosphere on Proxima Centauri b (assuming it is Earth-like) could be characterized at S/N = 5 in 20–30 hr of integration time. These observations would be particularly sensitive to CH_4, but CO_2 would be harder to detect.

While these previous studies have made significant contributions to assessing direct imaging capabilities for individual cases, they were intrinsically constrained in their scope for broader hypothesis testing. Our study seeks to build upon the above foundational efforts by employing the `Bioverse` framework, which allows us to go beyond previous studies by leveraging exoplanet demographics information, and performing realistic survey simulations and hypothesis testing.

1.2. `Bioverse`

`Bioverse` was developed by A. Bixel & D. Apai (2021) as a modular framework to generate and classify exoplanets based on exoplanet demographics, simulate exoplanet surveys for upcoming telescopes and missions, and compute the diagnostic power of future surveys in testing population-level hypotheses. `Bioverse` folds in state-of-the-art exoplanet occurrence rate calculations, incorporates a complete nearby star catalog out to ∼100 pc (Gaia red-band magnitude range $0.5 < G_{RP} < 19.9$), and accounts for realistic ground-based observing constraints, allowing exploration of the full potential of a broad statistical survey of nearby exoplanets.

The general workflow of `Bioverse` starts with generating synthetic populations of stars with planetary systems and to injecting a statistical trend into that population. Then, a simulated survey "observes" a sample of the synthetic planets and collects measurement data according to projected uncertainties and survey strategies. Next, the hypothesis testing module allows quantification of how well the injected trend is recovered, and how strongly the parameters of the model shaping the trend can be constrained. This procedure is typically repeated in a Monte Carlo fashion, varying astrophysical unknowns or features of the survey, which allows for trade studies on different survey designs.

After introducing the framework in A. Bixel & D. Apai (2021), K. K. Hardegree-Ullman et al. (2023) added a stellar catalog based on Gaia Data Release 3, with the capability to determine transit observability for ground-based large-aperture telescopes, and simulations for oxygen detection via transmission spectroscopy. M. Schlecker et al. (2024) introduced selectable mass–radius relations, a mission simulator for ESA's PLATO mission (H. Rauer et al. 2016), and a runaway greenhouse climate model. Here, we built upon these previous studies to assess the direct imaging and high-resolution spectroscopy potential for reflected-light studies with the GMT and ELT, specifically focusing on the ability to probe Earth-like O_2 levels. Leveraging all modules of `Bioverse`, we seek to test the "habitable zone oxygen hypothesis," i.e., the hypothesis that Earth-sized planets within a star's habitable zone are more likely to have Earth-like O_2 levels. This will inform us if a hypothetical 10 yr survey of exo-Earth candidates (EECs) with the ELT will be sufficient to test this hypothesis.

In Section 2 we outline the direct imaging observing considerations and instrument models. We simulate a 10 yr survey with the GMT and ELT to probe Earth-like levels of O_2 on habitable zone Earths and super-Earths in Section 3, and follow with testing the habitable zone oxygen hypothesis in Section 4. In Section 5 we discuss the implications of our simulations, and we summarize and conclude our results in Section 6.

2. Observing Considerations

Earth has evolved from a methane and carbon-dioxide-rich atmosphere over 2.4 Gyr ago to its present-day oxygen-rich state due to oxygenic photosynthesis (e.g., T. W. Lyons et al. 2021). While it is likely that habitable zone Earth-sized exoplanets have atmospheres with diverse compositions and in different states of evolution, we adopt present-day Earth as a starting point to simplify simulations. The following simulations are focused on probing present-day Earth-like atmospheric conditions on rocky, habitable zone exoplanets.

2.1. Planet Generation and Observational Constraints

In order to provide a realistic survey simulation, we used `Bioverse` to generate a set of exoplanets orbiting bright stars (Gaia red-band $G_{RP} \leqslant 10$) out to 20 pc from the Sun based on planet occurrence rates from G. J. Bergsten et al. (2022), which were first introduced to `Bioverse` in M. Schlecker et al. (2024). The underlying parametric model in G. J. Bergsten et al. (2022) is derived from the planet radius, orbital period, and stellar host mass distributions in Kepler's FGK and early M stars sample, considering planets with radii up to 3.5 $R_\oplus$ and orbiting out to 100 days. The original SAG 13–based (R. K. Kopparapu et al. 2018) planet occurrence rate module introduced by A. Bixel & D. Apai (2021) was derived from a compilation of Kepler planet occurrence rates prior to 2017, and did not include a stellar mass dependence. Both of the planet occurrence rate modules are model dependent for planets orbiting beyond 100 days. This does not affect our study much because an overwhelming majority of targets in our simulated surveys are M dwarfs (see Figure 5) with habitable zones closer than 100 days. We note that the SAG 13 occurrence rates are more optimistic than the G. J. Bergsten et al. (2022) values by a factor of ∼2, but we opt to use the G. J. Bergsten et al. (2022) values in this study because they are not only more recent, but also from a uniform study rather than a compilation.

From the set of generated exoplanets, we only considered planets that meet the criteria of an EEC: the planet is within the conservative habitable zone boundaries between runaway and maximum greenhouse as defined by R. K. Kopparapu et al. (2014), and the planet radius falls between the range $0.8S^{0.25} < R_p < 1.4\ R_\oplus$, where S is stellar incident flux in units of present-day Earth insolation flux. The lower limit is the theoretical minimum planet size needed to retain an atmosphere (K. J. Zahnle & D. C. Catling 2017), and was previously adopted for use in `Bioverse` by A. Bixel & D. Apai (2021) and K. K. Hardegree-Ullman et al. (2023).

In order to generate realistic surveys, for each EEC we simulated 1 Earth year of observations at 1 hr intervals and computed practical observing constraints based on the locations of the GMT and ELT. Simple constraints such as target observability at night and an airmass between $z = 1.0$ and 2.0 were modeled using `astroplan` (B. M. Morris et al. 2018).

When a planet was observable, we computed relative radial velocities and planet-to-star contrast ratios.

Since we have to observe O_2 on exoplanets through the O_2-rich atmosphere of Earth, we must account for relative radial velocities (ΔRV) in order to mitigate line blending effects. Relative radial velocities are given by:

$$\Delta RV = RV_\star + RV_{\rm orb} - RV_{\rm bary}, \quad (1)$$

where $RV_\star$ is the radial velocity of the host star, $RV_{\rm orb}$ is the orbital velocity of the exoplanet with respect to its host star, and $RV_{\rm bary}$ is the velocity of the observer on Earth with respect to the solar system barycenter. The host star radial velocity comes from the `Bioverse` stellar catalog (K. K. Hardegree-Ullman et al. 2023), which is based on Gaia Data Release 3. The uncertainties of these radial velocities are on the order of a few kilometers per second (Gaia Collaboration et al. 2021).

Orbital velocity was computed from:

$$RV_{\rm orb} = \sqrt{GM_\star\left(\frac{2}{r} - \frac{1}{a}\right)}, \quad (2)$$

where G is the gravitational constant, $M_\star$ is the mass of the host star, r is the distance of the exoplanet to the host star at the time of observation (computed in `Bioverse` using Newton's method to numerically solve Kepler's equation), and a is the semimajor axis of the exoplanet. Observer barycentric velocity at the time of observation was computed using the `baryCorr` function from the `PyAstronomy` package (S. Czesla et al. 2019). For an $R = 100{,}000$ spectrograph observing the O_2 A band, severe line blending occurs when $|\Delta RV| < 13\ {\rm km}^{-1}$ and $30\ {\rm km\ s}^{-1} < |\Delta RV| < 55\ {\rm km\ s}^{-1}$ (M. López-Morales et al. 2019; K. K. Hardegree-Ullman et al. 2023).

For direct imaging observations, the projected distance of the exoplanet from its host star (θ [arcsec] $= r$ [au]$/d$ [pc], where d is the distance to the system) must be larger than the inner working angle of the observing instrument. The diffraction limit of a telescope is $1.22\lambda/D$. In practice, we set the observable inner working angle to be greater than $2\lambda/D$ (e.g., C. Lovis et al. 2017; A. B. Walter et al. 2020). At the wavelength of the O_2 A band (760 nm), $2\lambda/D$ is 13 mas, 11 mas, and 9 mas for the GMT, TMT, and ELT, respectively.

In order to observe the exoplanet, the contrast ratio between the planet and the star must be above the detection limit of the instrument. This contrast ratio is given by:

$$C = \frac{F_p(\lambda, \alpha)}{F_\star(\lambda)} = A_g(\lambda) g(\alpha)\left(\frac{R_p}{a}\right)^2, \quad (3)$$

where $F_p(\lambda, \alpha)$ is the exoplanet flux at wavelength λ and phase angle α, $F_\star(\lambda)$ is the host star flux, A_g is the geometric albedo, $g(\alpha)$ is the scattering phase function, R_p is the exoplanet radius, and a is the exoplanet semimajor axis. Our models assume a Lambertian phase function:

$$g(\alpha) = \frac{\sin\alpha + (\pi - \alpha)\cos\alpha}{\pi}, \quad (4)$$

where the illumination phase angle $\alpha = \cos^{-1}(-\sin i \cos\phi)$, i is the exoplanet inclination angle, and ϕ is the orbital phase. Geometric albedo and inclination angle were randomly generated from uniform distributions for each simulated planet within `Bioverse`, and orbital phase was computed at 1 hr intervals by summing the argument of periastron and the mean anomaly, assuming the longitude of the ascending node is zero (in the direction toward the observer). The argument of periastron and mean anomaly are generated in `Bioverse` from uniform random distributions between zero and 2π and the mean anomaly is updated at 1 hr intervals, accounting for the simulated planet orbital period.

2.2. Instrument Models

In order to provide a realistic simulation of extreme-AO performance, we need models for planned instruments, which currently include GMagAO-X (J. R. Males et al. 2022) for the GMT and the Planetary Camera and Spectrograph (PCS; M. Kasper et al. 2021) for the ELT. However, full end-to-end simulations of these high-order AO systems are very expensive in terms of computational time and complexity. Therefore, we used a semianalytical approach to the performance simulation (L. Jolissaint 2010). The semianalytical approach assumes that all temporal evolution of the turbulence is driven by Taylor's frozen flow. The frozen flow approximates the short time evolution by shifting the spatial structure of the turbulence with a single-wind velocity. The time evolution of any parameter, f for example, can then be replaced by a shifted version, $f(\boldsymbol{r}, t) = f(\boldsymbol{r} - \boldsymbol{v}t)$. This time evolution underpins the semi-analytical model and allows us to express an AO system as a series of spatial filters that act on the turbulence power spectral density (PSD). The spatial frequency approach has been verified extensively in comparison with full end-to-end models (J. R. Males et al. 2021). The AO system is controlled using integral control, $\mathrm{DM}_{i+1} = \mathrm{DM}_i - g\varepsilon_i$. Here, ε_i is the wave front error at time step i and DM_i is the deformable mirror (DM) shape at time step i. The feedback gain g is a function of spatial frequency and was optimized following E. Gendron & P. Léna (1994) and L. Jolissaint (2010).

We simulated two different representative optimizations of the AO system. In the first, the AO system was allowed to run as fast as possible, which is 3 kHz for both GMagAO-X and PCS. The gain for each spatial frequency was optimized at this AO loop speed. In the second approach, we optimized the Strehl ratio by changing both the AO loop speed and modal gains. These two approaches were used because optimizing for only the Strehl ratio does not necessarily lead to the best contrast. The contrast at small angular separations is driven by the servo lag error. This error term is a larger contributor on GMT/ELT-sized instruments than on current instruments (J. R. Males & O. Guyon 2018). Therefore, it is possible to increase the contrast at smaller angular separations by running the AO system faster at the cost of a lower Strehl ratio. This leads to a better final S/N. The two different approaches are called "Max Speed" and "Strehl Optimization" in this work. A more thorough assessment of which instrument and observing modes were selected for scientific analysis in Section 3 is given in the Appendix.

AO performance strongly depends on the atmospheric conditions assumed. For our simulations, we followed G. Prieto et al. (2010) and J. E. Thomas-Osip et al. (2010) for the GMT (see Table 1). The first quartile conditions have a Fried parameter of $r_0 = 0.22$ m and a C_n^2 integrated wind velocity of $9.4\ {\rm m\ s}^{-1}$. Here C_n^2 is the refractive index structure parameter. The second quartile conditions are $r_0 = 0.17$ m and a mean wind speed of $18.4\ {\rm m\ s}^{-1}$. For the ELT, we followed

Table 1
Parameters Used to Calculate the Signal-to-noise Ratio (Equation (5))

ELT Parameters	
Telescope area	978 m^2
Number of actuators	128/200
Number of wave front sensor (WFS) pixels	125,000
GMT Parameters	
Telescope area	358 m^2
Number of actuators	188
Number of WFS pixels	111,000
Shared AO System Parameters	
Zero-point flux in *I* band	4520 photons s^{-1} cm^{-2} nm^{-1}
Bandwidth *I* band	150 nm
WFS wavelength	765 nm
Loop speed	250–4000 Hz
Intrinsic delay	1.5 frames
Computational delay	250 μs
Throughput to WFS camera	10%
WFS detector variance	2.0 e^-
Photon noise sensitivity	$1/\sqrt{2}$
Read noise sensitivity	$1/\sqrt{2}$
Common path throughput to spectrograph	25 %
Coronagraph	Fourth-order perfect coronagraph (O. Guyon et al. 2006)
Site Parameters	
r_0	10–20 cm
L_0	25 m
v	15–40 m s^{-1}
Spectrograph Parameters	
Read noise	1 e^- $pixel^{-1}$
Dark current	10^{-4} e^- s^{-1} $pixel^{-1}$
Spectrograph throughput	35%
Detector quantum efficiency	86%
Science wavelength	765 nm
Spectral bandwidth	10 nm
Resolving power	100,000–500,000
Spectral resolution	Three channels per resolving element
Pixels per channel	2 pixels

M. Sarazin et al. (2013): the first and second quartile conditions are $r_0 = 0.24$ m with a velocity of 10 m s^{-1} and $r_0 = 0.15$ m with a velocity of 11 m s^{-1}, respectively.

The design of GMagAO-X is currently further along than that of the other extreme-AO systems (S. Y. Haffert et al. 2024; J. R. Males et al. 2024). Therefore, we used the current design parameters for GMagAO-X as reference. Specifically, we assumed 188 actuators across the pupil and a pyramid WFS. The design of PCS is currently still in its conceptual phase and no hard decisions have been made (M. Kasper et al. 2021). Therefore, we considered two different DM sizes for PCS: 200 actuators across the pupil based on the proposed density for EPICS (M. Kasper et al. 2010), and 128 actuators across the pupil based on a more recent ELT extreme-AO design (P.-Y. Madec et al. 2022).

The output of the semianalytical model is a post-AO PSD. The PSD still has to be propagated through an actual coronagraphic system to measure the amount of residual scattered starlight. The expected exposure times of our simulations are on the order of hours. This is much longer than the typical speckle lifetime of 1–10 ms (J. R. Males et al. 2021). We can treat the different spatial frequencies as incoherent because of the many orders of magnitude differences in the characteristic timescales. With that in mind, the propagation through a coronagraph can be viewed as an incoherent sum of plane waves (J.-F. Sauvage et al. 2010; O. Herscovici-Schiller et al. 2017). The theoretical perfect coronagraph removes only the piston mode from the incoming wave front (O. Guyon et al. 2006; N. Deshler et al. 2024). However, such coronagraphs are extremely sensitive to residual jitter and partially resolved stars (O. Guyon et al. 2006). Therefore, we used a fourth-order perfect coronagraph that also removes the tip/tilt modes from the wave fronts beside the piston mode. This increases the inner working angle of the coronagraph and it increases the system robustness against stellar angular diameter and residual tip/tilt jitter (O. Guyon et al. 2006; R. Belikov et al. 2021). Given the size of the GMT/ELT, it will not be realistic to work with a second-order coronagraph that only removes pistons. Finally, the effects of time varying quasi-static speckles are ignored in the simulations for two reasons. For high-resolution spectroscopy, the only thing that matters is the amount of starlight that is left in the final spectra. The cross-correlation function is differentiating between stellar residuals and planet light through spectral information only and the associated noise is photon noise of the time-integrated spectrum intensity (I. Snellen et al. 2015). The speckle lifetime affects the variance of this intensity but not the mean (shorter lifetime → smaller variance/mean). We assume that the quasi-static speckles can be controlled and removed to a level that is below the halo of residual atmospheric speckles using newly implemented focal plane wave front control techniques (A. Potier et al. 2022; S. Haffert et al. 2023; R. Galicher et al. 2024) and that means the photon noise from the atmospheric speckles will dominate the noise budget. Therefore, the total power of the low-spatial frequency content of the quasi-static speckles was set to 1 nm and the high-spatial frequency content was set to 25 nm and added to our simulations. This amount is similar to what has been achieved with MagAO-X (K. Van Gorkom et al. 2021). We also assume that the efficiency of the quasi-static speckle removal process will continue to improve over the next few years. An example output of the semianalytical modeling is shown in Figure 1.

In order to calculate the S/N of the high-contrast, high-resolution spectroscopic observations of the exoplanet atmosphere O_2 *A* band, we follow the basic principle of I. Snellen et al. (2015) and C. Lovis et al. (2017):

$$\mathrm{S/N} = \frac{\eta \Delta t T_p T_I T_{\mathrm{AO}} T_{\mathrm{QE}} \mathrm{CF}_\star}{\sqrt{\Delta t T_\star T_I T_{\mathrm{AO}} T_{\mathrm{QE}} F_\star + \Delta t \sigma^2_{\mathrm{sky}} + N_{\mathrm{exp}} N_{\mathrm{pixels}} \sigma^2_{\mathrm{read}} + N_{\mathrm{pixels}} \Delta t \sigma^2_{\mathrm{dark}}}}. \quad (5)$$

The main difference between this equation and previous equations (I. Snellen et al. 2015; C. Lovis et al. 2017) is the parameterization of the planet signal after postprocessing. Earlier work used the combination of the average depth of the spectral line δ and the number of spectral lines N_{lines} to estimate the planet signal. However, this does not capture how postprocessing affects the line flux, which is the thing that we are sensitive to. High-resolution spectroscopy in direct imaging uses spectral high-pass filters to filter away stellar speckles. High spectral resolution features are then mostly left

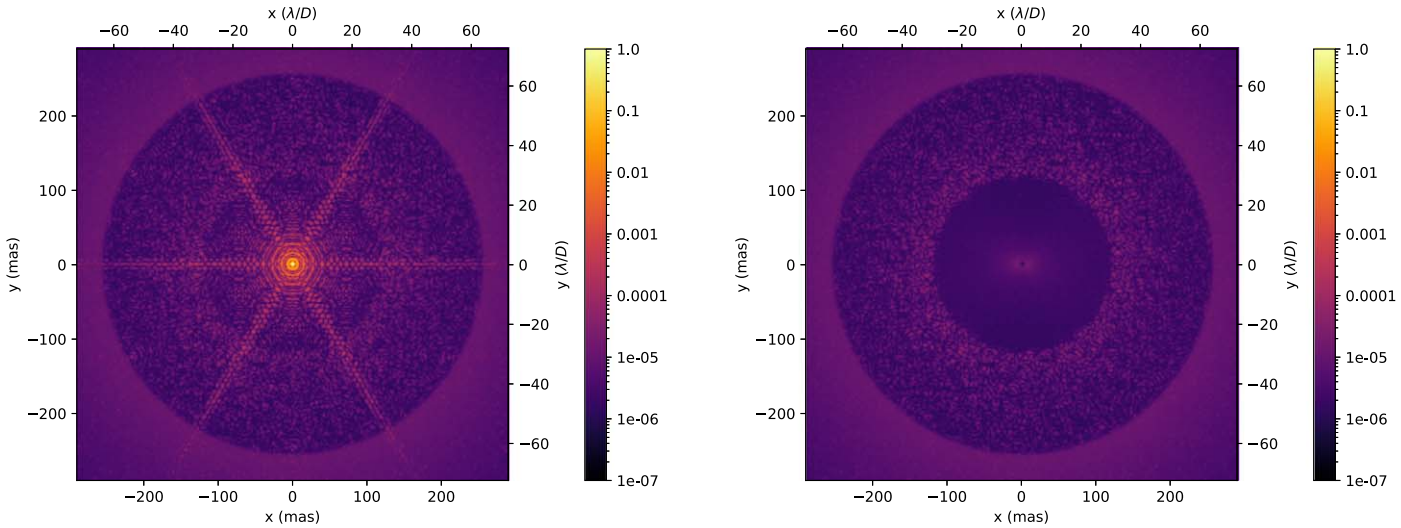

Figure 1. Output of the semianalytical AO simulations for ELT/PCS with the 128 actuator model. The left figure shows the simulated point-spread function (PSF) and the right figure shows the coronagraphic stellar image. There are two visible circular regions. The largest corresponds to the control radius of the AO system and the smaller one corresponds to the control radius of the non-common-path aberrations. The contrast within the inner radius is dominated by the wind-driven halo. Axes are shown in both milliarcseconds and λ/D, assuming $\lambda = 765$ nm and $D = 39.3$ m.

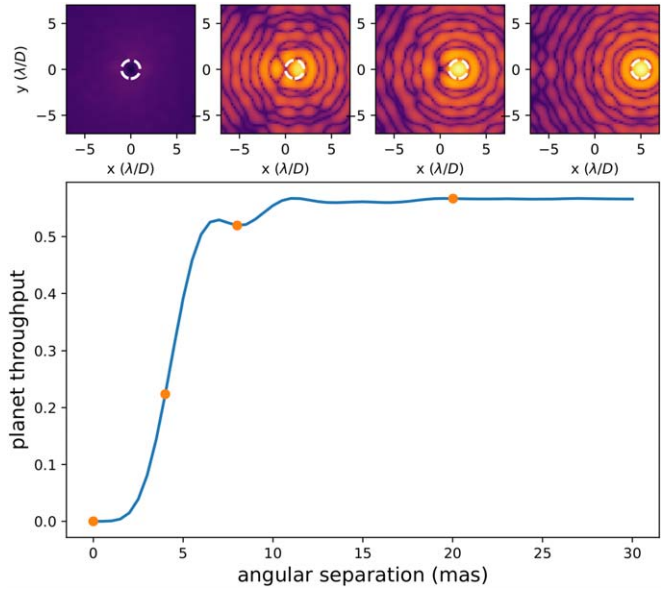

Figure 2. Coronagraphic encircled energy throughput ($1.8\lambda/D$ diameter) as a function of angular separation for an 8 mag star. A fourth-order perfect coronagraph with the ELT aperture was used in these simulations. The top row shows the PSFs corresponding to the four orange points on the throughput curve from 0 mas (left) to 20 mas (right) separation. The PSF is deformed close to the inner working angle of the coronagraph.

alone. In our new approach, we measure the power of the planet signal before and after the spectral high-pass filtering and then use the ratio to estimate how much of the signal is retained. This ratio is the postprocessing efficiency parameter η (J. Fowler et al. 2023). At high spectral resolution ($R > 100{,}000$), the planetary oxygen line signal is almost completely retained. This leads to a high postprocessing efficiency of 95%. A caveat for this number is that it depends on the spectral bandwidth of the measurement. The signal that we measure is completely contained by oxygen spectral lines. Over a wide spectral bandwidth the efficiency drops because we remove all broadband continuum features (due to the spectral high-pass filter). Therefore, 95% efficiency is achieved

Table 2
End-to-end GMagAO-X Planet Throughput in Percentages (from 0% to 100%) for Different Host Star Magnitudes and Planet–Star Angular Separations (θ)

	GMT, Max Speed, Q1					
Mag|θ	5 mas	10 mas	15 mas	30 mas	50 mas	120 mas
1	0.57	3.43	3.63	3.78	3.84	3.84
3	0.57	3.40	3.60	3.74	3.80	3.81
5	0.55	3.29	3.48	3.63	3.68	3.69
7	0.48	2.90	3.07	3.19	3.24	3.25
9	0.30	1.78	1.88	1.96	1.99	1.99
10	0.16	0.94	1.00	1.04	1.06	1.06

Note. This table is for a Max Speed AO control system and first quartile (Q1) observing conditions. For different AO control systems and observing conditions see Table 5 in the Appendix.

only in a 10 nm bandwidth centered around the oxygen A band. The other parameters in the equation are Δt, the total exposure time and T_p, the amount of light that is injected into a $1.8\lambda/D$ sized light bucket (e.g., an optical fiber or integral-field unit spaxel) after AO correction and through a coronagraph. Figure 2 shows how this throughput varies with off-axis angle for an 8 mag primary star, and Table 2 shows how the throughput varies for GMagAO-X for different magnitude primary stars. There are several places where flux is lost: the throughput losses in the spectrograph itself, T_I, the throughput through the common path optics of the AO system, $T_{\rm AO}$, and the quantum efficiency of the detector $T_{\rm QE}$. The planet-to-star contrast is C (Equation (3)), $F_\star$ is host star flux across the O_2 A band (10 nm bandwidth) at the top of Earth's atmosphere, $T_\star$ is the stellar throughput measured at the location of the planet in the $1.8\lambda/D$ sized aperture, and $\sigma^2_{\rm sky}$, $\sigma^2_{\rm read}$, and $\sigma^2_{\rm dark}$ are the sky background noise, detector read noise, and dark current noise, per pixel, respectively. The spectra are sampled by $N_{\rm pixels}$ per spectral channel and the observation is broken up into $N_{\rm exp}$ exposures per hour of observing time. Our approach to the analytical modeling of high-resolution spectroscopy almost exactly follows the work of R. Landman et al. (2023), J. Fowler et al. (2023), and A. Bidot et al. (2024). A. Bidot et al. (2024)

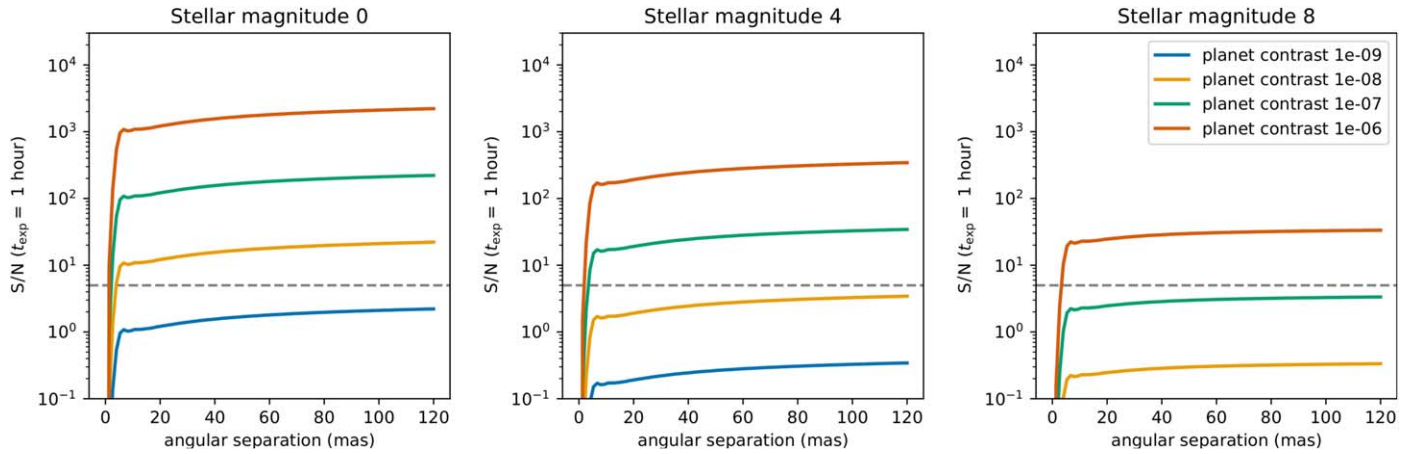

Figure 3. The S/N after a 1 hr integration for different planet contrasts and stellar magnitudes. The S/N = 5 detection limit is shown by the dashed gray line.

Table 3
GMT Achievable $F_p/F_\star$ Contrast at a Signal-to-noise Ratio of Five for 1 hr Integration Times Using High-contrast Imaging with High-resolution Spectroscopy for Different Host Star Magnitudes and Planet–Star Angular Separations (θ)

	GMT, Max Speed, Q1					
Mag|θ	5 mas	10 mas	15 mas	30 mas	50 mas	120 mas
1	3.06E–08	6.09E–09	5.85E–09	4.53E–09	3.51E–09	2.35E–09
3	9.79E–08	1.97E–08	1.93E–08	1.61E–08	1.32E–08	9.50E–09
5	4.01E–07	8.10E–08	8.00E–08	6.88E–08	5.83E–08	4.39E–08
7	2.26E–06	4.57E–07	4.54E–07	4.00E–07	3.47E–07	2.71E–07
9	2.12E–05	4.30E–06	4.30E–06	3.87E–06	3.43E–06	2.72E–06
10	8.87E–05	1.80E–05	1.81E–05	1.65E–05	1.49E–05	1.15E–05

Note. This table is for a Max Speed AO control system and Q1 observing conditions. For different AO control systems and observing conditions see Table 5 in the Appendix.

Table 4
ELT Achievable $F_p/F_\star$ Contrast at a Signal-to-noise Ratio of Five for 1 hr Integration Times Using High-contrast Imaging with High-resolution Spectroscopy for Different Host Star Magnitudes and Planet–Star Angular Separations (θ)

	ELT, Max Speed, 128 actuators, Q1					
Mag|θ	5 mas	10 mas	15 mas	30 mas	50 mas	120 mas
1	2.55E–09	2.08E–09	1.99E–09	1.55E–09	1.25E–09	9.36E–10
3	7.12E–09	5.84E–09	5.64E–09	4.64E–09	3.90E–09	2.95E–09
5	2.48E–08	2.04E–08	1.99E–08	1.68E–08	1.43E–08	1.09E–08
7	1.03E–07	8.49E–08	8.30E–08	7.14E–08	6.17E–08	4.78E–08
9	5.72E–07	4.72E–07	4.64E–07	4.06E–07	3.57E–07	2.82E–07
10	1.62E–06	1.34E–06	1.32E–06	1.17E–06	1.03E–06	8.24E–07

Note. This table is for a Max Speed AO control system, 128 deformable mirror actuators, and Q1 observing conditions. For different AO control systems, actuators, and observing conditions see Table 7 in the Appendix.

also find that semianalytical modeling of the cross-correlation postprocessing results in the exact same performance as full end-to-end modeling. We used the designs of the RHEA and RISTRETTO spectrographs (A. D. Rains et al. 2016; M. Bugatti et al. 2024) as a guide for our chosen spectrograph performance requirements (see Table 1).

At high resolution ($R \geqslant 100{,}000$), we can mitigate Earth's telluric signal by avoiding observing the exoplanet at relative radial velocities at which line blending is severe (Section 2.1). Disentangling the star and exoplanet signal happens in postprocessing by cross correlating the reflected-light spectrum with the stellar spectrum. The cross-correlation postprocessing efficiency (η) for the O_2 A band converges to 95% for $R \geqslant 100{,}000$ (J. Fowler et al. 2023) if the planet is sufficiently Doppler shifted (K. K. Hardegree-Ullman et al. 2023). Rearranging Equation (5), we computed the achievable contrast C at S/N = 5 for 1 hr total integration times (assuming four 15 minute exposures) for different host star apparent magnitudes and angular separations for the GMT (Table 3) and ELT (Table 4). The brightest stars might require shorter exposures,

but the dominant detector noise will be dark current, which scales with exposure time, rather than read noise, so the effect is insignificant.

There are several caveats to these simulations. First, there is no variability of the atmospheric conditions during a single observation. Variability is expected to lower the effective performance. However, we simulated the end-to-end yield in first quartile Q1 and second quartile Q2 conditions and these are used as upper and lower bounds on the performance. Later results will also show that the unknowns in the astrophysical statistics are dominating the yield estimates. Second, we assume that we reach the photon- or detector-noise-dominated regime. This means that we assume little to no covariance between the spectral channels. This might seem optimistic, but H. J. Hoeijmakers et al. (2018) reached a postprocessing contrast of $\sim 10^{-5}$ by combining a significant amount of data from many different seeing-limited instruments, while the proposed survey will need to reach 10^{-3}–10^{-4}. Reaching the noise limits does require correct O_2 models for the cross correlation because model imperfections will lead to lower efficiency (S. R. Vaughan et al. 2024). However, the O_2 transmission spectrum of the HITRAN model is generally very accurate because it predicts the atmospheric tellurics to a high precision (I. Gordon et al. 2022).

2.3. Time Needed to Probe O_2

With our new instrument model, we now have to determine how long it will take to probe O_2. For each simulated exoplanet, we first computed the total number of hours the planet would be observable from the GMT and ELT locations for 1 yr of observations ($N_{\text{hr-obs}}$) accounting for the aforementioned ground-based observing limitations and exoplanet orbital properties. Since the modeled planets change illumination and scattering phase throughout their orbits, we computed the contrast ratio from Equation (3) at each observable hour and used the resulting median contrast ratio ($\widetilde{F_p/F_\star}$) for our calculations. Tables 3 and 4 show the expected achievable postprocessing contrasts from the instrument models in Section 2.2 for the GMT and ELT, respectively, at $S/N = 5$ for a 1 hr integration of the O_2 A band at $R = 100{,}000$ for different host magnitudes and angular separations.

It would be ideal to optimize observations based on maximizing Equation (3). However, this depends on several factors, including well-constrained exoplanet orbits and phases and appropriate relative system velocities coinciding with Q1 or Q2 observing windows. It is impractical to assume observations will only happen when all these factors are most optimal, so we opted for a more conservative median observing situation. For each simulated exoplanet, we interpolated the host star G_{RP} magnitude and median angular separation ($\tilde{\theta}$) to these tables to yield a 1 hr contrast ($C_{1\text{ hr}}$). The total integration time to achieve an $S/N = 5$ detection of Earth-like levels of O_2 on the simulated planet ($t_{\text{hr-}5\sigma}$) is given by:

$$t_{\text{hr-}5\sigma} = \left(\frac{C_{1\text{ hr}}}{\widetilde{F_p/F_\star}} \right)^2. \tag{6}$$

To translate the total integration time to years of observations, we need to account for both target observability ($N_{\text{hr-obs}}$) and acceptable site observing conditions (Q):

$$t_{\text{yr-}5\sigma} = Q \frac{t_{\text{hr-}5\sigma}}{N_{\text{hr-obs}}}, \tag{7}$$

where $Q = 4$ for first quartile observing conditions (best observing site weather, ideal for extreme AO, ~25% of telescope observing time, will take 4 times longer to achieve the required S/N) and $Q = 2$ for second quartile observing conditions (best to average observing site weather, ~50% of telescope observing time, will take twice as long to achieve the required S/N). It is worth emphasizing that $N_{\text{hr-obs}}$ only counts times at which the relative system velocities yield unblended lines and the planet is observable from the observing site. We simulate first and second quartile observing conditions for each instrument mode, and assess the trade-offs of different observing scenarios in the Appendix.

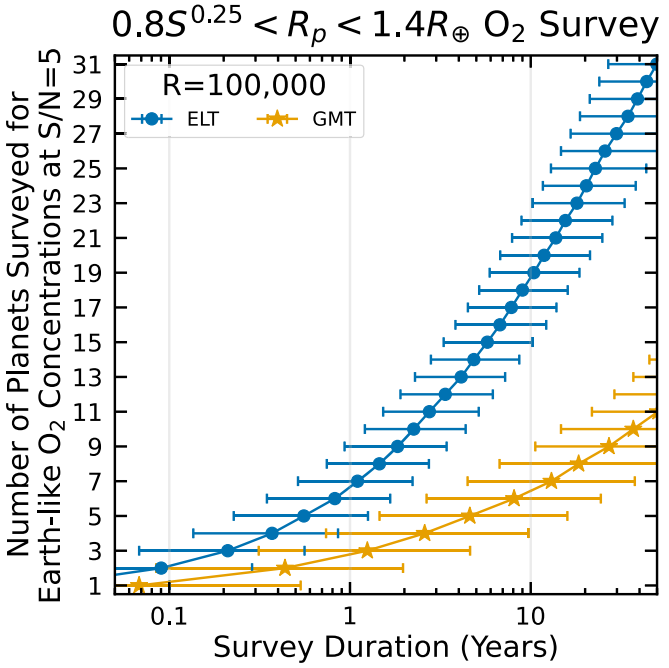

Figure 4. Simulation results for a survey of Earth-like concentrations of O_2 at $S/N = 5$ on EECs within 20 pc with the ELT (blue dots) and the GMT (orange stars). A survey of the same duration on both telescopes would allow the ELT to probe about 3 times more planets for O_2 than the GMT. The large error bars are driven by the wide range of possible orbital parameters for our simulated exoplanets.

3. Survey Simulation

In order to realistically simulate the execution of an observing survey of nearby EECs, we followed the survey simulation methodology of K. K. Hardegree-Ullman et al. (2023). First, we generated 1000 simulated local neighborhood ($d < 20$ pc) exoplanet populations in `Bioverse` based on the exoplanet demographics of G. J. Bergsten et al. (2022) and computed the time it will take to probe Earth-like O_2 levels for each simulated EEC. We then sorted each population of simulated exoplanets by the number of years it would take to probe O_2 and calculated the median value of the first through nth planets. The results are shown in Figure 4 for optimized instrument and observing modes, which are Max Speed, Q1 for the GMT, and Max Speed, Q1, 128 actuators for the ELT. An

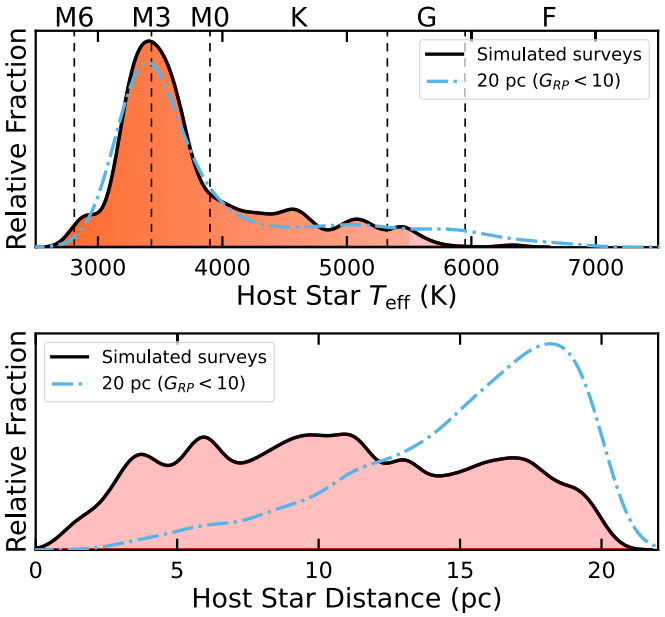

Figure 5. Distributions of host star $T_{\rm eff}$ (top) and distance (bottom) across all EEC survey simulations for EECs that could be probed for Earth levels of O_2 within a 10 yr survey. 85% of the detectable simulated planets orbit M dwarfs, with a peak near spectral type M3. About three-quarters of the detectable simulated planets are within 13 pc of the Sun. The dashed–dotted blue lines show the distribution of all bright ($G_{\rm RP}$ < 10) stars within 20 pc, which highlights that the GMT and ELT will be insensitive to O_2 in the atmospheres of EECs orbiting stars above ∼5000 K, and is most sensitive to stars within about 13 pc.

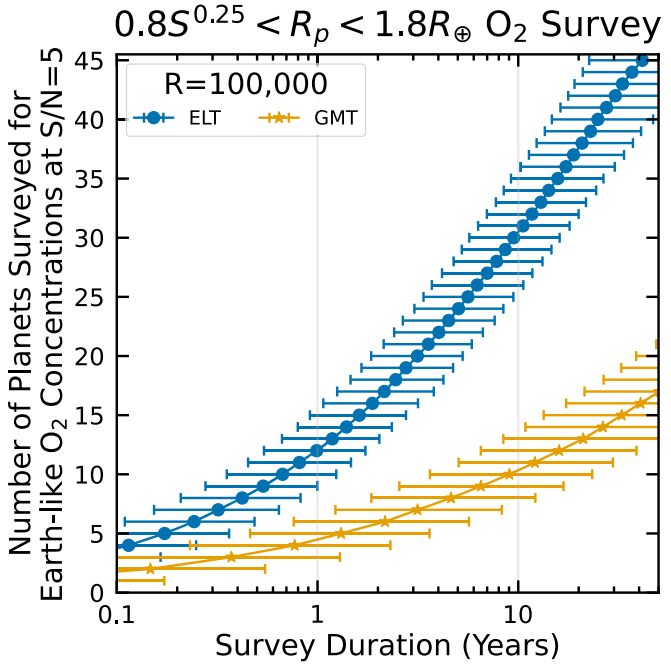

Figure 6. Simulation results for a survey of Earth-like concentrations of O_2 at S/N = 5 on habitable zone Earth and super-Earth-sized candidates ($0.8S^{0.25} < R_p < 1.8\ R_\oplus$) within 20 pc with the ELT (blue dots) and the GMT (orange stars). Similar to the exo-Earth simulation in Figure 4, the ELT could probe about 3 times more planets than the GMT. Overall, a super-Earth survey could probe about 1.5 times more planets than a survey of planets up to 1.4 $R_\oplus$.

assessment of different instrument and observing modes is given in the Appendix.

Figure 4 shows that the ELT would be able to survey ∼3× more planets than the GMT for a survey of similar length, approximately commensurate with the ∼3× more collecting area. For example, in a 10 yr survey from start to finish, if all EECs have Earth-like levels of O_2, the GMT could probe up to ∼7 planets, and the ELT could probe up to ∼19. Note, that this simulation did not consider that these planets would likely have overlapping observing windows, so the number of planets surveyed for O_2 is an upper limit. Further observing optimization (e.g., observing exoplanets near maximum phase, or combining measurements from multiple telescopes) should be possible, but was not explored in this study. It is also important to highlight that over 85% of the simulated planets which could be probed within a 10 yr survey across all survey simulations orbit M dwarfs, and about 75% of these simulated planets are within 13 pc of the Sun (Figure 5).

3.1. Super-Earths

Next, we carried out a simulation to explore the observability of O_2 in all super-Earth exoplanets. The previous survey simulation focused on planets nearly the same size as Earth ($0.8S^{0.25} < R_p < 1.4\ R_\oplus$). While not all exoplanets smaller than 1.4 $R_\oplus$ will necessarily be Earth-like, a larger population including all super-Earth exoplanets would allow us to observationally constrain the limits of Earth-like planet atmospheres. In the following simulation, we assessed the ability to probe Earth-like O_2 levels on Earth- to super-Earth-sized planets ($0.8S^{0.25} < R_p < 1.8\ R_\oplus$), where the upper limit is guided by the exoplanet radius valley (B. J. Fulton et al. 2017;

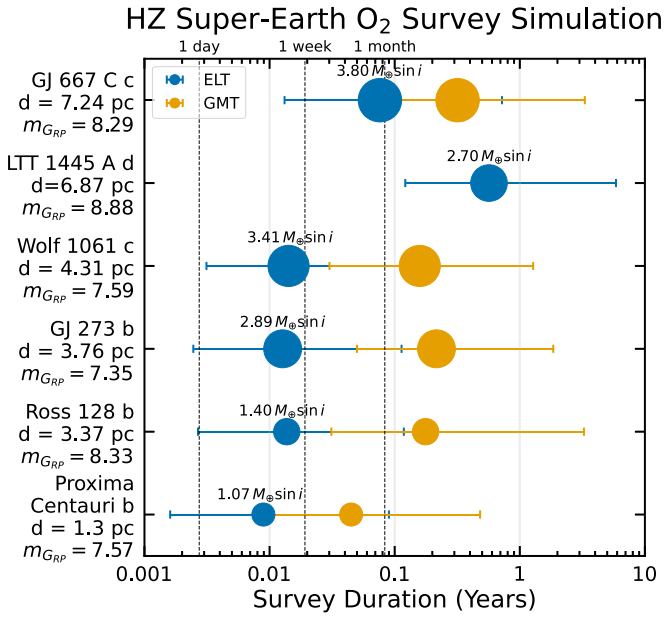

Figure 7. Simulation results for a survey of Earth-like concentrations of O_2 at S/N = 5 for five known, and one candidate (LTT 1445 A d), habitable zone exoplanets within 20 pc with the ELT (blue) and the GMT (orange). The ELT and GMT should both be able to probe for O_2 on Proxima Centauri b in less than a month. LTT 1445 A d is the only planet in the simulation for which Earth-like levels of O_2 could not be probed with the GMT, but it could be probed with the ELT. More precise planet and orbital parameters would minimize the uncertainties on these observing simulations. The minimum mass ($M_\oplus \sin i$) of each planet is given above each relatively sized point (Anglada-Escudé et al. 2013; N. Astudillo-Defru et al. 2017; X. Bonfils et al. 2018; J. P. Faria et al. 2022; B. Lavie et al. 2023).

K. K. Hardegree-Ullman et al. 2020). Results from the super-Earth survey simulation are given in Figure 6. We found that about 1.5× more planets could be surveyed if the survey is broadened from Earth-sized to all Earth- and super-Earth-sized planets.

3.2. Known Habitable Zone Exoplanets

Within 20 pc there are five confirmed habitable zone exoplanets which would be observable from either the GMT or ELT. These exoplanets orbit stars brighter than $G_{RP} = 10$ and have minimum masses ($M \sin i$) that make them super-Earth candidates. These are Proxima Centauri b (G. Anglada-Escudé et al. 2016), Ross 128 b (X. Bonfils et al. 2018), GJ 273 b (N. Astudillo-Defru et al. 2017), Wolf 1061 c (D. J. Wright et al. 2016), and GJ 667 C c (G. Anglada-Escudé et al. 2012). LTT 1445 A d is another nearby candidate super-Earth habitable zone exoplanet with a relatively bright host star (B. Lavie et al. 2023). It is worth noting that all these planets were discovered orbiting M dwarfs using the radial velocity technique, and it is possible that their mass is significantly higher than the minimum mass provided by the radial velocity method (see, e.g., A. Bixel & D. Apai 2017). We ran a survey simulation on these planets, assuming uniform priors on all unknown or loosely constrained parameters such as albedo, inclination angle, argument of periastron, and longitude of the ascending node. Results from this simulation are shown in Figure 7. If Earth-like levels of O_2 exist on these planets, they could be probed within days to a few weeks with the ELT, and within a couple of months with the GMT. For LTT 1445 A d, it will take several months, and can only be completed on the ELT within a 10 yr survey. Given the fact that the existence of these planets is already established, they will likely be high-priority targets for initial exoplanet surveys with the GMT and ELT.

4. Hypothesis Testing

Since our survey simulations revealed the possibility of detecting O_2 on several exoplanets in a 10 yr survey, particularly with the ELT, in order to assess the scientific value of such surveys, we now turn to testing related population-level hypotheses. We refer the reader to Section 5 of A. Bixel & D. Apai (2021) for a full description of Bayesian hypothesis testing with `Bioverse`. In general, we want to assess the statistical power of a survey to test a hypothesis by running survey simulations several times in a Monte Carlo fashion under the same assumptions (but with randomly drawn parameters) and determine the fraction of simulations that validate or reject the hypothesis. Here, we propose and aim to test the "habitable zone oxygen hypothesis:" we hypothesize that habitable zone Earth-sized exoplanets will be more likely to have Earth-like levels of O_2 than planets outside the habitable zone.

We must first define the statistical effect to inject into our synthetic planet population. In our model, a planet can have or not have Earth-like levels of O_2. It can further be an EEC if its orbit fulfills $a_{inner} < a < a_{outer}$ and its radius fulfills $0.8S^{0.25} < R_p < 1.4\ R_\oplus$. The planet is considered a non-EEC otherwise, but its atmosphere may still contain Earth-like levels of oxygen. This population of oxygen-bearing non-EECs can be considered false positives, and they present a source of noise in the hypothesis testing.

We can now describe the likelihood of a planet having O_2 by:

$$f^{O_2} = \begin{cases} f^{O_2}_{EEC} & \text{if } a_{inner} < a < a_{outer}, \\ & \text{and } 0.8S^{0.25} < R_p < 1.4\ R_\oplus, \\ f^{O_2}_{non\text{-}EEC} & \text{if } a < a_{inner} \text{ or } a > a_{outer}, \\ & \text{and } R_p > 0.8S^{0.25}, \\ 0 & \text{if } R_p < 0.8S^{0.25}, \end{cases} \quad (8)$$

where $f^{O_2}_{EEC}$ is the fraction of EECs with Earth-like O_2 levels, and $f^{O_2}_{non\text{-}EEC}$ is the fraction of non-habitable-zone exoplanets with O_2.

Next, we adopt the functional form of the habitable zone oxygen hypothesis, $H^{O_2}_{HZ}$, as:

$$H^{O_2}_{HZ}(a_{eff}) = \begin{cases} f^{O_2}_{HZ} & \text{if } a_{inner} < a_{eff} < a_{inner} + \Delta a, \\ f^{O_2}_{HZ}\,(f^{O_2}_{non\text{-}HZ}\,/f^{O_2}_{HZ}) & \text{otherwise.} \end{cases} \quad (9)$$

The model parameter vector θ consists of the position of the inner edge of the habitable zone a_{inner}, the width of the habitable zone Δa, the fraction of habitable zone planets with O_2 $f^{O_2}_{HZ}$, and the ratio of non-habitable-zone planets with O_2 to habitable zone planets with O_2 $f^{O_2}_{non\text{-}HZ}\,/f^{O_2}_{HZ}$.

In our test case, we aim to assess the statistical power to test the above hypothesis in a 10 yr survey with the ELT considering different values of $f^{O_2}_{EEC}$ (10 levels between 0.1 and 1) and $\eta_\oplus$ (five levels between 0.075 and 0.3). For simplicity, we set $f^{O_2}_{non\text{-}EEC} = 1\%$. A higher value of $f^{O_2}_{non\text{-}EEC}$ would inject more false-positive O_2 signals and skew our results to require fewer detections to test our hypothesis. We intentionally keep this value low because future surveys, like the one used in this hypothesis test, will likely only probe planets within the habitable zone defined either by incident stellar flux levels, or confirmed with liquid water detections on the habitable zone planets. We imposed log-uniform priors $a_{inner} = [0.1, 2]$, $\Delta a = [0.01, 3]$, $f_{HZ} = [0.01, 1]$, and $f_{non\text{-}HZ}/f_{HZ} = [0.01, 1.0]$.

For each of these realizations, our planetary populations are still subject to intrinsic stochasticity that may impact the measured diagnostic power of the survey: planetary orbits and bulk properties are randomly drawn from distributions informed by exoplanet demographics, leading to random variations of the sample. To account for this while keeping computational costs reasonable, we ran 10 randomized simulations per grid cell.

Figure 8 shows the statistical power that can be achieved for different fractions of EECs with Earth-like levels of O_2 and $\eta_\oplus$. Our ability to test the habitable zone oxygen hypothesis is contingent on more than ∼one-third of EECs having Earth-like levels of O_2 if EECs are relatively common, and above ∼one-half for low values of $\eta_\oplus$. Figure 6 suggests that a 10 yr survey of exo-super-Earth candidates (ESECs) could probe about 1.5× more planets for Earth-like levels of O_2 than a survey of only Earth-sized planets. As such, we ran the above test with the same parameters except considering ESECs rather than EECs. Figure 8 shows that considering ESECs would not necessarily improve the ability to test the habitable zone oxygen hypothesis. One potential reason for this is that in a time-limited ground-based survey, a larger target sample would take longer to survey a significant fraction and test the hypothesis. A higher-resolution hypothesis grid with more samples per cell

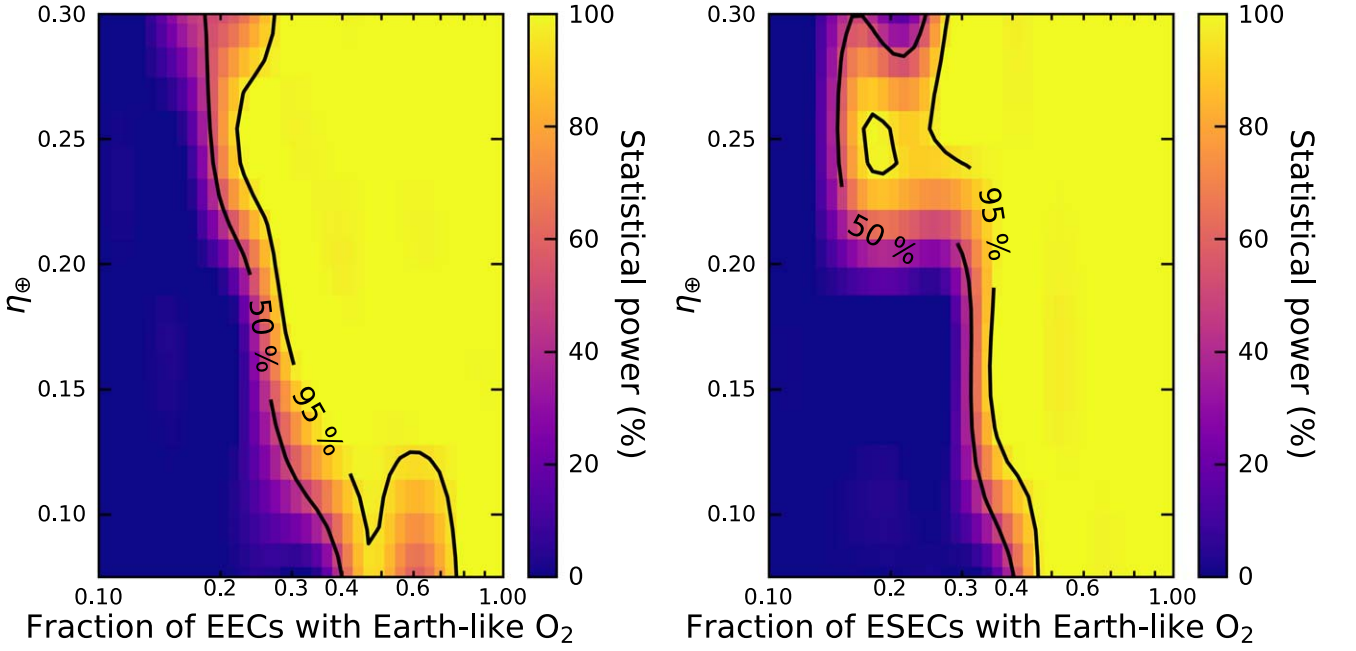

Figure 8. Statistical power of the habitable zone oxygen hypothesis test on the ELT for different values of $\eta_\oplus$ and different fractions of EECs (left) and fractions of ESECs (right) with Earth-like levels of O_2. Statistical power contours for 50% and 95% are shown in black. More planets with oxygen and/or higher values for $\eta_\oplus$ result in a greater ability to test this hypothesis, however, the inclusion of all super-Earths does not necessarily improve this ability. We note that these figures are supersampled to highlight differences.

could test this more conclusively, but that is significantly more computationally expensive.

In the previous two hypothesis tests, we considered $f_{\mathrm{EEC}}^{\mathrm{O_2}}$ or $f_{\mathrm{ESEC}}^{\mathrm{O_2}}$ for planets up to 1.4 $R_\oplus$ (EEC) and 1.8 $R_\oplus$ (ESEC) for different values of $\eta_\oplus$. Next, instead of varying $\eta_\oplus$, we set $\eta_\oplus = 8.5\%$ (consistent with the most recent estimates of $\eta_\oplus$ for conservative habitable zone M dwarfs from G. J. Bergsten et al. 2023) and tested the effect of maximum sampled planet size on our ability to test the habitable zone oxygen hypothesis. Figure 9 shows the results of this test, indicating the maximum sampled planet size has only a small effect on the ability to test the habitable zone oxygen hypothesis between ~1.2 $R_\oplus$ and 1.8 $R_\oplus$.

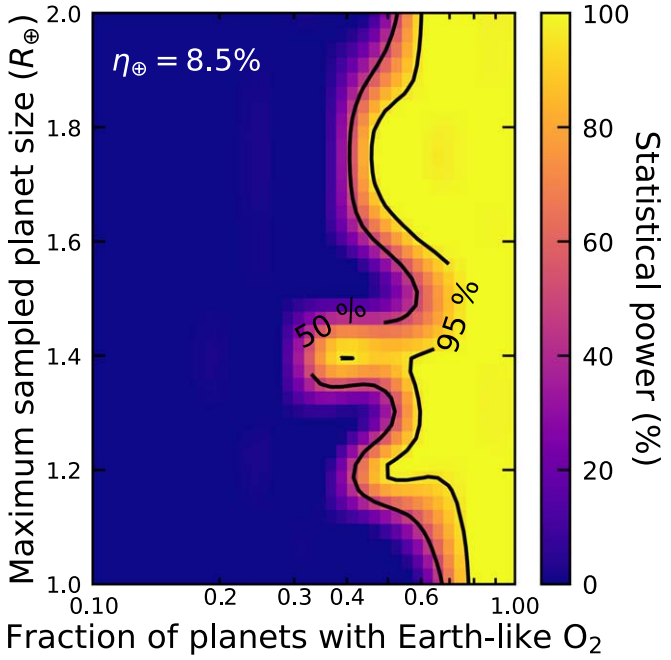

Figure 9. Statistical power of the habitable zone oxygen hypothesis test on the ELT for different values of maximum sampled planet size and different fractions of planet candidates with Earth-like levels of O_2. Statistical power contours for 50% and 95% are shown in black. The maximum sampled planet size has a minor effect on the statistical power between ~1.2 $R_\oplus$ and ~1.8 $R_\oplus$. We note that this figure is supersampled.

5. Discussion

The detection of O_2 in the atmospheres of Earth analogs, if found, will no doubt have profound impacts on astronomy and astrobiology. Our simulations show that Earth-like O_2 levels could be probed on EECs with the GMT and ELT with planned instrumentation. There are already a half dozen known probable super-Earths which may be ideal candidates to start searching for oxygen (Section 3.2), and planets like Proxima Centauri b could be high-priority science targets for the GMT and ELT. Below we discuss simulation limitations and survey feasibility, O_2, other biosignatures, and the importance of population-level biosignature interpretation, and end with a brief discussion of the TMT.

5.1. Limitations and Survey Feasibility

Our simulations are based on loosely constrained (e.g., $\eta_\oplus$) or unknown astrophysical parameters (e.g., orbital parameters). These contribute significantly to the uncertainties of our survey simulations. Exoplanet occurrence rate studies with TESS, Roman, and PLATO, and radial velocity surveys to find new EECs around nearby stars could help further reduce survey uncertainties and find new candidates for biosignature searches.

It is important to note that the GMT and ELT will be mostly sensitive to exoplanets orbiting M dwarf stars (Figure 5), and particularly those in the habitable zone. These exoplanets will not be accessible to the HWO, which is expected to primarily

focus on Sun-like FGK stars (E. Mamajek & K. Stapelfeldt 2024). The nature of the habitability of M dwarf exoplanets is extensively studied in the literature (e.g., A. L. Shields et al. 2013, 2016; V. S. Meadows et al. 2018a; V. S. Airapetian et al. 2020; A. H. Lobo et al. 2023) and is beyond the scope of this paper.

Since the extreme-AO systems for the ELTs are still in their planning stages, we rely on instrument parameters that are not yet finalized or that are based on current systems. Consequentially, our simulations can also be used to provide guidance to instrument teams as to the requirements for biosignature searches with the ELTs.

In Section 3, we did not consider that multiple target planets could be observable at the same time, or by multiple ELTs. We also used the median calculated contrast ratio for each simulated planet (using only contrast ratios for the times the planets were observable in 1 yr of simulated observations). For simulation purposes, these are reasonable assumptions to provide upper limits to yields for an exoplanet biosignature survey for individual telescopes.

Our 10 yr survey assumed we would observe during Q1 observing conditions. Since the ELTs are not solely dedicated to exoplanet science, it is unlikely that all Q1 observing time would be dedicated to the search for biosignatures; though, exoplanets are not always observable or at ideal phases for direct imaging during Q1 observing conditions. As we assess in the Appendix, it makes little difference whether a survey is conducted in Q1 or Q2 observing conditions, which would likely be a factor in designing a biosignature survey. Until additional nearby EECs are identified, we can only report upper limits to survey yields for a hypothetical observing scenario as presented here.

5.2. O_2 as an Atmospheric Biosignature

Life on Earth has a complex evolutionary history with O_2. About 2.4 billion years ago, cyanobacteria took in solar energy and produced O_2 as a waste product of oxygenic photosynthesis. Eventually, enough oxygen had accumulated in the ocean to begin escaping into the atmosphere during the "Great Oxidation Event," ushering in the Proterozoic Eon and the evolution of complex life. A second great atmospheric accumulation of oxygen occurred between about 800 and 600 million years ago, leading to present-day levels of oxygen and animal life (D. E. Canfield 2005; L. R. Kump 2008; A. L. Sessions et al. 2009; T. W. Lyons et al. 2014, 2021). In this study, we focused on the ability to probe present-day Earth-like levels of O_2 on rocky exoplanets. From 600 Mya to present day, Earth oxygen levels fluctuated between ∼10% and 30%, settling at ∼21% today (K. M. Costa et al. 2014). W. G. Chaloner (1989) suggest that O_2 concentrations of ∼35% are the upper limit to sustain terrestrial vegetation due to the increased potential for combustibility. We leave the exploration of the limits of O_2 detectability to future studies.

5.3. Other Atmospheric Biosignatures

O_2 on Earth is almost exclusively produced by oxygenic photosynthesis (A. Segura et al. 2005), and its present-day abundance, which is difficult to replicate by individual abiotic mechanisms (V. S. Meadows 2017), makes it a favorable biosignature to search for in the atmospheres of exoplanets. However, there are still mechanisms that could produce an oxygen-rich atmosphere, such as water photolysis on a pure H_2O world (R. Wordsworth & R. Pierrehumbert 2014). This necessitates robust elimination of false-positive abiotic O_2 production scenarios. One way to do this is by observing multiple biosignatures (V. S. Meadows et al. 2018b).

CH_4 is another exoplanet biosignature candidate, as its primary production mechanism on Earth is from methanogenic bacteria in anaeorbic environments (A. Segura et al. 2005; R. K. Thauer & S. Shima 2008). Abiotic CH_4 can be produced by volcanic and geothermal processes, or by gas–water–rock reactions (G. Etiope & B. Sherwood Lollar 2013; A. Guzmán-Marmolejo et al. 2013), but on Earth, biological production of CH_4 outweighs abiotic production by an order of magnitude (D. S. Kelley et al. 2005; A. Segura et al. 2005). The thermodynamic disequilibrium of CH_4 and O_2 on Earth (D. R. Hitchcock & J. E. Lovelock 1967; C. Sagan et al. 1993), makes the disequilibrium pair a particularly enticing biosignature. Additionally, for M dwarf planets, which will be the primary targets for biosignature searches via direct imaging with the GMT and ELT, the photochemical lifetime of CH_4 is ∼200 yr, compared to ∼10 yr on Earth (A. Segura et al. 2005; G. N. Arney 2019), which might make it easier to detect on such planets.

CO_2 and CH_4 are another disequilibrium pair that may indicate life. This pair is particularly important for exoplanets with an Archean-like atmospheric composition when those two species dominated in the O_2-deficient environment (J. D. Haqq-Misra et al. 2008). CH_4 could be produced abiotically via mantle outgassing, but this would also produce abundant CO (J. Krissansen-Totton et al. 2018). A biologically active planet would likely have depleted CO levels because this would be the preferred energy source for methanogens over CO_2, making the absence of CO a biological check on the CO_2–CH_4 pair (K. Zahnle et al. 2011; J. Krissansen-Totton et al. 2018).

Figure 10 shows the habitable zone accessibility of the biosignatures O_2, CH_4, CO_2, and CO at red optical and near-infrared wavelengths for an inner working angle of $2\lambda/D$ for the GMT, TMT, ELT, and JWST/HWO at distances of 5 and 10 pc. We have also included H_2O, which is the basis of our definition of a habitable zone planet (R. K. Kopparapu et al. 2014). Our study focused on the O_2 *A* band at 0.76 μm, which could be probed in the atmospheres of most inner habitable zone planets orbiting stars up to M4 V by the GMT, TMT, and ELT out to ∼10 pc. Toward near-infrared wavelengths, the inner working angle decreases, diminishing the ability to probe some bands of biosignatures such as CO and CO_2 in the atmospheres of exoplanets orbiting later-type and more distant stars. We leave the exploration of the ability to probe other biosignatures with the GMT, TMT, and ELT to future studies.

5.4. A Statistical Interpretation of Biosignatures

Even if it is possible to probe multiple biosignatures on an exoplanet, interpretation of detections/nondetections on a single planet will vary (see, e.g., N. Madhusudhan et al. 2023; S.-M. Tsai et al. 2024; N. F. Wogan et al. 2024). Therefore, it is crucial to survey a large number of planets to study biotic and abiotic processes and interpret biosignatures statistically (D. Apai et al. 2019). Here, we focused on the potential to probe Earth-like levels of O_2 on a statistical level on hypothetical nearby exoplanets using direct imaging and high-resolution spectroscopy. Studying exoplanets on a population level with large-aperture ground-based telescopes

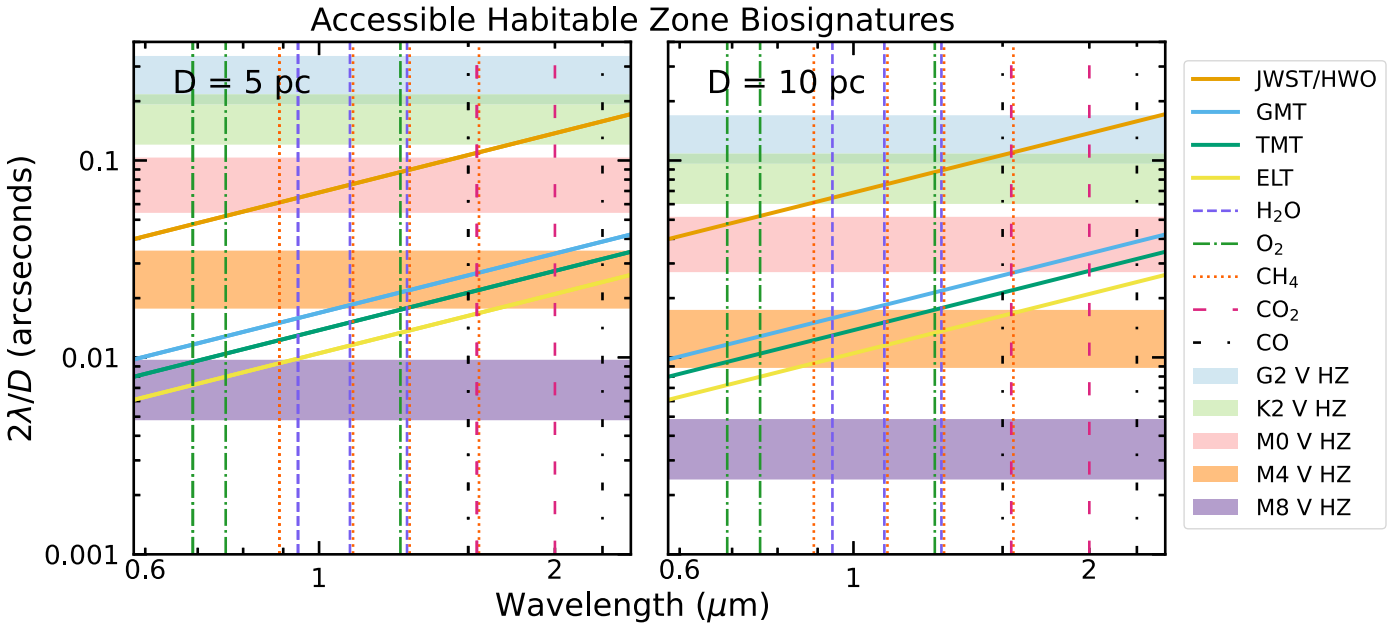

Figure 10. The inner working angles at $2\lambda/D$ for 0.6–2 μm are plotted for an ∼6 m JWST or anticipated HWO diameter aperture (orange solid line), the GMT (blue solid line), the TMT (green solid line), and the ELT (yellow solid line). The wavelengths of H_2O (blue dashed), O_2 (green dashed–dotted), CH_4 (orange dotted), CO_2 (pink dashed), and CO (black dotted) for this wavelength region are plotted as vertical lines. The plot considers distances of 5 pc (left) and 10 pc (right). The shaded horizontal regions show the conservative habitable zones for representative G2 V through M8 V stars. If a habitable zone region falls above the inner working angle of a telescope, an exoplanet and its biosignatures should be observable at that wavelength range. For example, below 1 μm, the GMT should be able to observe O_2, CH_4, and H_2O for planets in the habitable zones of a hypothetical M4 V star at 5 pc. The GMT will only be able to access biosignatures between 1 and 2 μm if planets fall in certain regions of the habitable zone of this hypothetical star, and it will not be able to access biosignatures beyond 2 μm.

will allow testing of the habitable zone oxygen hypothesis and other statistical trends connected to small-planet atmosphere diversity and planet formation processes.

5.5. TMT

The TMT is the only 25–40 m class telescope planned for the Northern Hemisphere. It should be noted that there are about 9700 stars within 20 pc of the Sun brighter than 10 mag above a decl. of 30°. This is about 25% of bright, nearby stars which are inaccessible to the GMT and ELT. A Northern Hemisphere large-aperture telescope is critical to maximize the search for biosignatures. Additionally, about two-thirds of the targets observable from a large-aperture telescope at 20° or 30° latitude overlap with the targets observable from the GMT and ELT in the Southern Hemisphere.

Having multiple facilities capable of searching for biosignatures is advantageous. When we are looking for $S/N = 5$ biosignature detections over years of observations and hundreds of data sets, it will be important to have independent verification from, e.g., different telescopes and processing techniques to minimize false-positive scenarios. Multiple facilities can both expedite data collection on individual targets and potentially expand the target pool amenable to biosignature surveys if data from different instruments can be combined, and since weather conditions at one facility become less of an observing bottleneck. H. J. Hoeijmakers et al. (2018) successfully demonstrated combining more than 2000 high-resolution reflected-light spectra from different 2–8 m class telescopes to measure the albedo of the hot Jupiter τ Boötis b and achieved a planet-to-star contrast of $\sim 10^{-5}$. The GMT, TMT, and ELT will be able to build upon these methods to reach smaller planets and potentially detect biosignatures.

The Planetary Systems Imager (PSI) is a planned second-generation instrument for the TMT which will have extreme-AO and high-resolution spectroscopic capabilities (R. Jensen-Clem et al. 2021, 2022). We did not model the potential of TMT + PSI in this paper because a detailed instrument model is not yet available. However, assuming similar performance to the ELT and GMT systems, the TMT could probe a ∼50% larger sample than the GMT and—equivalently—probe a sample ∼66% the size of the ELT sample in a 10 yr survey, commensurate with the difference in telescope collecting area.

6. Summary and Conclusions

The `Bioverse` survey simulation and hypothesis testing framework enables comprehensive and quantitative assessments of the capabilities of upcoming ground-based telescopes and space missions to study exoplanets. We expanded the `Bioverse` framework to assess the ability of the ELT and the GMT to probe Earth-like levels of O_2 on nearby (<20 pc) habitable zone Earth-sized exoplanets via extreme-AO direct imaging and high-resolution spectroscopy. The following list summarizes the main conclusions of this work.

1. Accounting for recent planet occurrence rate calculations, relative system velocities, and realistic target observability, we conducted a survey simulation to determine how many exo-Earths ($0.8S^{0.25} < R_p < 1.4\ R_\oplus$) and super-Earths ($0.8S^{0.25} < R_p < 1.8\ R_\oplus$) could be probed for Earth-like levels of O_2 at $S/N = 5$ with the GMT and ELT. In 10 yr, the GMT could survey up to ∼7 and ∼10 Earths and super-Earths, respectively, while the ELT could survey up to ∼19 and ∼31, respectively (Figures 4 and 6).
2. Six known, habitable zone super-Earth candidates (Proxima Centauri b, Ross 128 b, GJ 273 b, Wolf 1061 c,

LTT 1445 A d, and GJ 667 C c) are ideal targets to search for O_2. Given favorable orbital and exoplanet atmosphere parameters, Earth-like levels of O_2 could be probed in a matter of about 1 week to a few weeks of observing for four of these planets with the ELT, and about a month with the GMT (Figure 7).
3. A 10 yr survey with the ELT could determine if habitable zone exo-Earths are more likely to have O_2. The diagnostic power of the survey to test this habitable zone oxygen hypothesis is sensitive to the fraction of EECs with Earth-like levels of O_2 and the value of $\eta_\oplus$, but not very sensitive to maximum planet size (Figures 8 and 9).
4. The construction of a Northern Hemisphere large-aperture telescope like the TMT would increase the potential target star sample by 25%. Multiple facilities can provide independent verification of biosignature detections, expedite data collection on individual exoplanets, and potentially expand the exoplanet target sample on which to search for biosignatures.

The upcoming 25–40 m class telescopes are going to be the first facilities capable of robustly detecting biosignatures with extreme-AO direct imaging and high-resolution spectroscopy. This method is much more promising than transmission spectroscopy in the search for O_2 (K. K. Hardegree-Ullman et al. 2023), and a handful of high-priority target planets are already available. The ability to validate biosignature detections and test the habitable zone oxygen hypothesis and other biosignature hypotheses, however, depends on probing a larger sample of planets than has been currently discovered.

Acknowledgments

We acknowledge the work of Bryan Wang to improve the `Bioverse` code. K.K.H.-U. acknowledges Megan Weiner Mansfield for general discussions about M dwarf exoplanet atmospheres and Suri Rukdee for discussions about the LTT 1445 A system. We thank the anonymous referee for their helpful comments, which significantly improved the clarity of this manuscript.

This material is based upon work supported by the National Aeronautics and Space Administration under Agreement No. 80NSSC21K0593 for the program "Alien Earths." The results reported herein benefited from collaborations and/or information exchange within NASA's Nexus for Exoplanet System Science (NExSS) research coordination network sponsored by NASA's Science Mission Directorate.

This material is based upon High Performance Computing (HPC) resources supported by the University of Arizona TRIF, UITS, and Research, Innovation, and Impact (RII) and maintained by the University of Arizona Research Technologies department.

This research has made use of NASA's Astrophysics Data System.

Software: `astroplan` (B. M. Morris et al. 2018), `astropy` (Astropy Collaboration et al. 2013, 2018, 2022), `Bioverse` (A. Bixel & D. Apai 2021; K. K. Hardegree-Ullman et al. 2023; M. Schlecker et al. 2024), `dynesty` (J. S. Speagle 2020), `matplotlib` (J. D. Hunter 2007), `numpy` (C. R. Harris et al. 2020), `pandas` (W. McKinney 2010; pandas Development Team 2020), `PyAstronomy` (S. Czesla et al. 2019).

Author Contributions

K.K.H.-U. and D.A. developed the project and planned its implementation. D.A. funded the project through the "Alien Earths" program and provided regular feedback and guidance as the project progressed. K.K.H.-U. updated the `Bioverse` code, performed the calculations and analysis, and drafted the manuscript. S.Y.H. created the GMT and ELT instrument models and computed contrast tables for O_2. M.S. assisted with `Bioverse` code issues and hypothesis test implementation. M.K. provided early models of PCS performance. M.K. and J.K. gave project input regarding the ELT and hypothesis testing. K.W. provided guidance on practical direct imaging observations. All authors contributed suggestions and edits to the manuscript.

Appendix
Different Instrument Modes

For both the GMT and ELT, we first assessed different instrument setups and observing conditions. The GMagAO-X on GMT setup assumes a baseline number of 188 deformable mirror actuators, and we looked at two different AO control system optimization strategies: Max Speed and Strehl Optimization. For PCS on the ELT, additional calculations were made for both a 128 or 200 actuator setup. Table 5 shows results for the different AO control systems and observing conditions for the GMT, and Table 7 shows results for different AO control systems, actuator counts, and observing conditions for the ELT. For each of these setups, we also give the end-to-end planet throughput for different host star magnitudes and angular separations for the GMT/GMagAO-X in Table 6 and the ELT/PCS in Table 8.

Except for survey durations longer than 10 yr on the ELT, Max Speed yields faster O_2 detections than Strehl Optimization. There is a trade-off for observing in different conditions. Observing in Q2 conditions allows more observing time, but it will take longer to build up signal on a target. From these simulations, Q1 versus Q2 observing only makes marginal differences depending on the instrument setup. The large uncertainties (computed as the 16th and 84th percentiles of the first through nth planets in the sorted universes; see Figure 4 for typical uncertainties for all models) effectively place all instrument setup results within 1σ. Nonetheless, we selected the GMT Max Speed Q1 and the ELT Max Speed, 128 actuators, Q1 instrument setups to perform additional optimistic simulations due to their marginally better performance than the other instrument setups for surveys with a duration of up to 10 yr (Figure 11).

A higher-resolution spectrograph produces narrower and deeper absorption and emission lines. For O_2, higher resolution gives access to more relative system velocity space. We modeled an $R = 500{,}000$ spectrograph coupled to our AO systems, for which severe line blending in the O_2 A band occurs when $|\Delta RV| < 10\,\mathrm{km\,s^{-1}}$ and $40\ \mathrm{km\ s^{-1}} < |\Delta RV| < 48\,\mathrm{km\,s^{-1}}$ (M. López-Morales et al. 2019; K. K. Hardegree-Ullman et al. 2023). As noted by J. Fowler et al. (2023), the postprocessing efficiency does not change at $R > 100{,}000$, so we are able to use Tables 5 and 7 for our $R = 500{,}000$ calculations. The lower panel of Figure 11 shows the results for $R = 500{,}000$ compared to $R = 100{,}000$, with a $\sim$1 or two planet increase in planets surveyed for a survey of 10 yr.

Table 5

GMT Achievable $F_p/F_\star$ Contrast for a Signal-to-noise Ratio of Five for 1 hr Integration Times Using High-contrast Imaging with High-resolution Spectroscopy for Different Host Star Magnitudes and Planet–Star Angular Separations (θ)

	Max Speed, Q1						Max Speed, Q2					
Mag|θ	5 mas	10 mas	15 mas	30 mas	50 mas	120 mas	5 mas	10 mas	15 mas	30 mas	50 mas	120 mas
1	3.06E–08	6.09E–09	5.85E–09	4.53E–09	3.51E–09	2.35E–09	6.11E–08	1.27E–08	1.24E–08	9.52E–09	6.91E–09	4.04E–09
3	9.79E–08	1.97E–08	1.93E–08	1.61E–08	1.32E–08	9.50E–09	1.68E–07	3.48E–08	3.42E–08	2.76E–08	2.17E–08	1.49E–08
5	4.01E–07	8.10E–08	8.00E–08	6.88E–08	5.83E–08	4.39E–08	6.00E–07	1.25E–07	1.24E–07	1.07E–07	8.90E–08	6.54E–08
7	2.26E–06	4.57E–07	4.54E–07	4.00E–07	3.47E–07	2.71E–07	3.26E–06	6.74E–07	6.76E–07	6.00E–07	5.19E–07	4.02E–07
9	2.12E–05	4.30E–06	4.30E–06	3.87E–06	3.43E–06	2.72E–06	3.39E–05	6.99E–06	7.06E–06	6.44E–06	5.75E–06	4.62E–06
10	8.87E–05	1.80E–05	1.81E–05	1.65E–05	1.49E–05	1.15E–05	1.71E–04	3.52E–05	3.57E–05	3.32E–05	3.03E–05	2.40E–05
Mag	Strehl Optimization, Q1						Strehl Optimization, Q2					
1	3.88E–08	7.69E–09	7.33E–09	5.43E–09	3.92E–09	2.32E–09	6.11E–08	1.27E–08	1.24E–08	9.52E–09	6.91E–09	4.04E–09
3	1.46E–07	2.90E–08	2.77E–08	2.05E–08	1.48E–08	8.67E–09	2.07E–07	4.32E–08	4.22E–08	3.25E–08	2.38E–08	1.45E–08
5	7.34E–07	1.45E–07	1.38E–07	1.01E–07	7.15E–08	3.82E–08	1.04E–06	2.17E–07	2.11E–07	1.61E–07	1.15E–07	6.25E–08
7	2.53E–06	5.01E–07	4.77E–07	3.52E–07	2.53E–07	1.46E–07	4.08E–06	8.51E–07	8.30E–07	6.33E–07	4.55E–07	2.56E–07
9	1.34E–05	2.65E–06	2.52E–06	1.86E–06	1.32E–06	7.38E–07	1.83E–05	3.81E–06	3.72E–06	2.86E–06	2.09E–06	1.26E–06
10	2.30E–05	4.55E–06	4.35E–06	3.29E–06	2.48E–06	1.65E–06	5.29E–05	1.10E–05	1.08E–05	8.23E–06	5.96E–06	3.35E–06

Note. Tables are given for different AO control systems (Max Speed and Strehl Optimization) and Q1 and Q2 observing conditions.

Table 6
End-to-end GMagAO-X Planet Throughput in Percentages (from 0% to 100%) for Different Host Star Magnitudes and Planet–Star Angular Separations (θ)

	Max Speed, Q1						Max Speed, Q2					
Mag|θ	5 mas	10 mas	15 mas	30 mas	50 mas	120 mas	5 mas	10 mas	15 mas	30 mas	50 mas	120 mas
1	0.57	3.43	3.63	3.78	3.84	3.84	0.56	3.35	3.55	3.69	3.75	3.75
3	0.57	3.40	3.60	3.74	3.80	3.81	0.55	3.30	3.50	3.64	3.69	3.70
5	0.55	3.29	3.48	3.63	3.68	3.69	0.52	3.14	3.32	3.46	3.51	3.52
7	0.48	2.90	3.07	3.19	3.24	3.25	0.43	2.59	2.74	2.85	2.89	2.90
9	0.30	1.78	1.88	1.96	1.99	1.99	0.21	1.24	1.31	1.36	1.38	1.39
10	0.16	0.94	1.00	1.04	1.06	1.06	0.08	0.48	0.51	0.53	0.53	0.54
Mag	Strehl Optimization, Q1						Strehl Optimization, Q2					
1	0.57	3.43	3.63	3.78	3.84	3.84	0.56	3.35	3.55	3.69	3.75	3.75
3	0.57	3.41	3.61	3.76	3.82	3.82	0.55	3.31	3.50	3.65	3.70	3.71
5	0.56	3.36	3.55	3.70	3.76	3.76	0.54	3.22	3.41	3.55	3.60	3.61
7	0.54	3.23	3.42	3.56	3.62	3.62	0.50	2.99	3.17	3.29	3.35	3.35
9	0.49	2.92	3.09	3.22	3.27	3.27	0.41	2.47	2.62	2.73	2.77	2.77
10	0.44	2.64	2.80	2.91	2.96	2.96	0.34	2.06	2.18	2.26	2.30	2.30

Note. Tables are given for different AO control systems (Max Speed and Strehl Optimization) and Q1 and Q2 observing conditions.

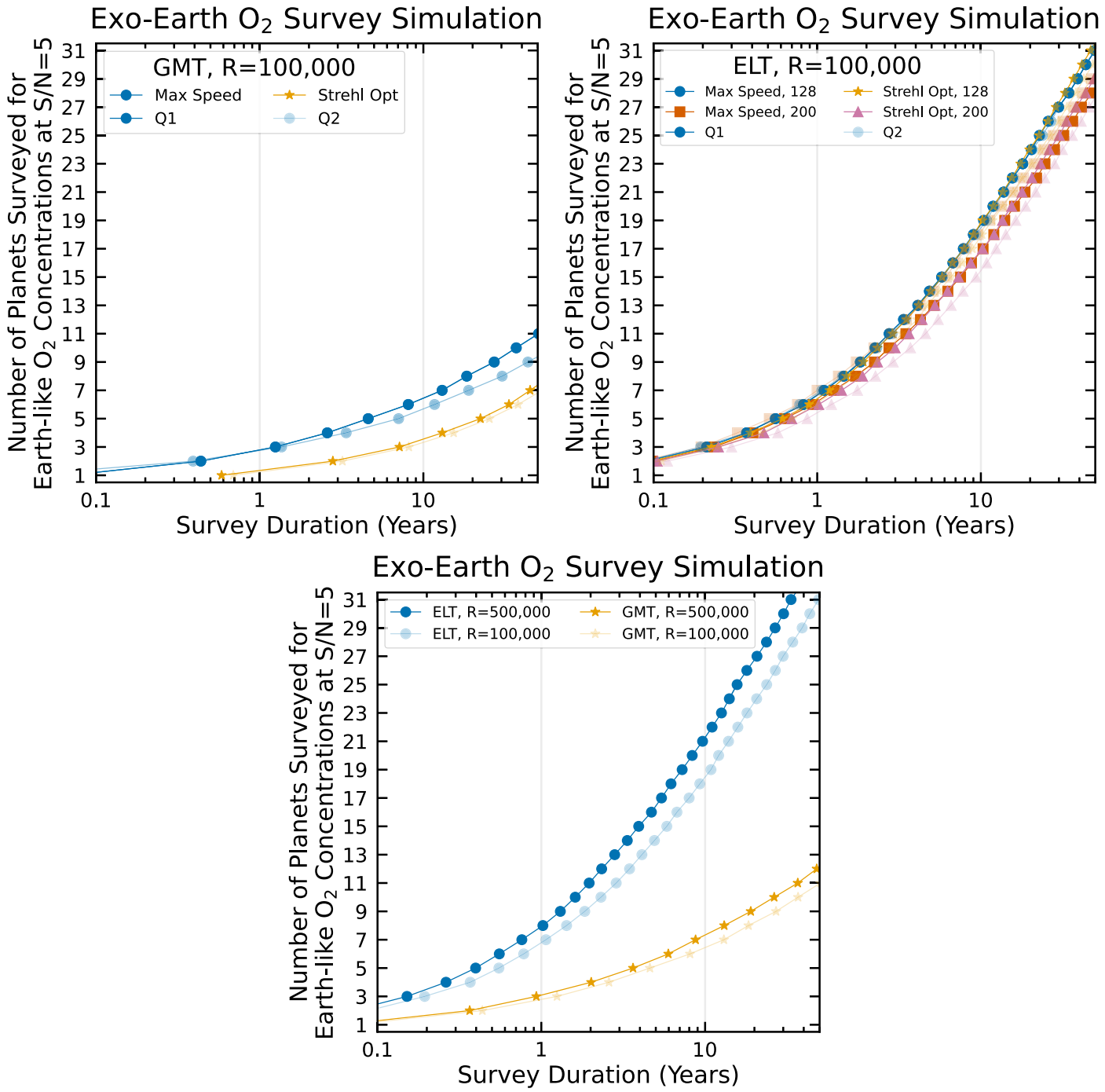

Figure 11. Simulation results for a survey of Earth-like O_2 levels at $S/N = 5$ of EECs within 20 pc with different AO control systems and observing conditions for the GMT (upper left), additionally accounting for different deformable mirror actuator counts on the ELT (upper right), and considering an optimized setup for both the GMT and ELT but assessing the differences between $R = 100{,}000$ and $R = 500{,}000$ (lower panel).

Table 7

ELT Achievable $F_p/F_\star$ Contrast for a Signal-to-noise Ratio of Five for 1 hr Integration Times Using High-contrast Imaging with High-resolution Spectroscopy for Different Host Star Magnitudes and Planet–Star Angular Separations (θ)

	Max Speed, 128 actuators, Q1						Max Speed, 128 actuators, Q2					
Mag|θ	5 mas	10 mas	15 mas	30 mas	50 mas	120 mas	5 mas	10 mas	15 mas	30 mas	50 mas	120 mas
1	2.55E–09	2.08E–09	1.99E–09	1.55E–09	1.25E–09	9.36E–10	5.00E–09	4.07E–09	3.89E–09	3.11E–09	2.58E–09	1.97E–09
3	7.12E–09	5.84E–09	5.64E–09	4.64E–09	3.90E–09	2.95E–09	1.30E–08	1.06E–08	1.02E–08	8.33E–09	7.06E–09	5.50E–09
5	2.48E–08	2.04E–08	1.99E–08	1.68E–08	1.43E–08	1.09E–08	3.91E–08	3.21E–08	3.12E–08	2.64E–08	2.26E–08	1.75E–08
7	1.03E–07	8.49E–08	8.30E–08	7.14E–08	6.17E–08	4.78E–08	1.49E–07	1.22E–07	1.19E–07	1.02E–07	8.82E–08	6.85E–08
9	5.72E–07	4.72E–07	4.64E–07	4.06E–07	3.57E–07	2.82E–07	7.95E–07	6.54E–07	6.41E–07	5.60E–07	4.91E–07	3.90E–07
10	1.62E–06	1.34E–06	1.32E–06	1.17E–06	1.03E–06	8.24E–07	2.34E–06	1.93E–06	1.89E–06	1.67E–06	1.49E–06	1.20E–06
Mag	Max Speed, 200 actuators, Q1						Max Speed, 200 actuators, Q2					
1	2.24E–09	1.83E–09	1.72E–09	1.27E–09	9.48E–10	6.18E–10	4.06E–09	3.33E–09	3.13E–09	2.27E–09	1.66E–09	1.01E–09
3	6.39E–09	5.24E–09	5.03E–09	4.02E–09	3.27E–09	2.31E–09	1.07E–08	8.77E–09	8.32E–09	6.31E–09	4.92E–09	3.39E–09
5	2.34E–08	1.93E–08	1.87E–08	1.56E–08	1.31E–08	9.73E–09	3.39E–08	2.79E–08	2.70E–08	2.21E–08	1.83E–08	1.33E–08
7	1.07E–07	8.78E–08	8.58E–08	7.37E–08	6.35E–08	4.89E–08	1.46E–07	1.20E–07	1.17E–07	9.95E–08	8.50E–08	6.46E–08
9	7.13E–07	5.88E–07	5.77E–07	5.07E–07	4.46E–07	3.52E–07	9.95E–07	8.22E–07	8.07E–07	7.07E–07	6.21E–07	4.93E–07
10	2.22E–06	1.83E–06	1.80E–06	1.60E–06	1.42E–06	1.13E–06	3.42E–06	2.82E–06	2.78E–06	2.48E–06	2.21E–06	1.78E–06
Mag	Strehl Optimization, 128 actuators, Q1						Strehl Optimization, 128 actuators, Q2					
1	2.55E–09	2.08E–09	1.99E–09	1.55E–09	1.25E–09	9.36E–10	5.00E–09	4.07E–09	3.89E–09	3.11E–09	2.58E–09	1.97E–09
3	8.29E–09	6.78E–09	6.44E–09	4.94E–09	3.91E–09	2.86E–09	1.57E–08	1.28E–08	1.21E–08	9.37E–09	7.48E–09	5.46E–09
5	3.03E–08	2.48E–08	2.35E–08	1.76E–08	1.36E–08	9.60E–09	5.62E–08	4.57E–08	4.30E–08	3.20E–08	2.44E–08	1.65E–08
7	1.46E–07	1.20E–07	1.13E–07	8.14E–08	5.90E–08	3.59E–08	1.88E–07	1.53E–07	1.44E–07	1.07E–07	8.11E–08	5.57E–08
9	5.94E–07	4.85E–07	4.57E–07	3.30E–07	2.40E–07	1.49E–07	9.28E–07	7.53E–07	7.06E–07	5.08E–07	3.68E–07	2.24E–07
10	1.20E–06	9.77E–07	9.20E–07	6.70E–07	4.93E–07	3.18E–07	1.81E–06	1.47E–06	1.38E–06	9.99E–07	7.34E–07	4.70E–07
Mag	Strehl Optimization, 200 actuators, Q1						Strehl Optimization, 200 actuators, Q2					
1	2.91E–09	2.37E–09	2.23E–09	1.59E–09	1.13E–09	6.42E–10	4.06E–09	3.33E–09	3.13E–09	2.27E–09	1.66E–09	1.01E–09
3	1.09E–08	8.92E–09	8.37E–09	5.96E–09	4.21E–09	2.33E–09	1.36E–08	1.11E–08	1.05E–08	7.58E–09	5.50E–09	3.35E–09
5	3.68E–08	3.01E–08	2.82E–08	2.02E–08	1.44E–08	8.38E–09	5.10E–08	4.18E–08	3.93E–08	2.83E–08	2.04E–08	1.21E–08
7	1.40E–07	1.14E–07	1.07E–07	7.72E–08	5.56E–08	3.33E–08	2.56E–07	2.10E–07	1.97E–07	1.40E–07	9.86E–08	5.33E–08
9	7.10E–07	5.79E–07	5.44E–07	3.88E–07	2.76E–07	1.56E–07	1.06E–06	8.70E–07	8.18E–07	5.84E–07	4.13E–07	2.29E–07
10	1.53E–06	1.25E–06	1.17E–06	8.40E–07	5.99E–07	3.46E–07	2.19E–06	1.79E–06	1.69E–06	1.21E–06	8.64E–07	4.99E–07

Note. Tables are given for different AO control systems (Max Speed and Strehl Optimization), 128 and 200 deformable mirror actuators, and Q1 and Q2 observing conditions.

Table 8
End-to-end ELT/PCS Planet Throughput in Percentages (from 0% to 100%) for Different Host Star Magnitudes and Planet–Star Angular Separations (θ)

	Max Speed, 128 actuators, Q1						Max Speed, 128 actuators, Q2					
Mag|θ	5 mas	10 mas	15 mas	30 mas	50 mas	120 mas	5 mas	10 mas	15 mas	30 mas	50 mas	120 mas
1	2.74	3.88	3.92	3.95	3.96	3.96	2.32	3.29	3.33	3.36	3.36	3.36
3	2.73	3.87	3.92	3.95	3.95	3.95	2.32	3.28	3.32	3.35	3.35	3.35
5	2.72	3.86	3.90	3.94	3.94	3.94	2.30	3.26	3.30	3.33	3.33	3.34
7	2.69	3.80	3.85	3.88	3.88	3.89	2.26	3.20	3.24	3.26	3.27	3.27
9	2.48	3.51	3.55	3.59	3.59	3.59	2.00	2.84	2.87	2.90	2.90	2.90
10	2.13	3.01	3.05	3.07	3.08	3.08	1.57	2.22	2.25	2.27	2.27	2.27
Mag	Max Speed, 200 actuators, Q1						Max Speed, 200 actuators, Q2					
1	2.94	4.16	4.21	4.25	4.25	4.25	2.74	3.88	3.93	3.96	3.97	3.97
3	2.93	4.15	4.20	4.24	4.24	4.24	2.73	3.87	3.92	3.95	3.95	3.95
5	2.91	4.12	4.17	4.21	4.21	4.21	2.70	3.83	3.88	3.91	3.91	3.91
7	2.82	4.00	4.04	4.08	4.08	4.08	2.58	3.65	3.70	3.73	3.73	3.73
9	2.37	3.36	3.40	3.43	3.43	3.43	1.92	2.73	2.76	2.78	2.79	2.79
10	1.88	2.66	2.69	2.71	2.72	2.72	1.26	1.78	1.80	1.82	1.82	1.82
Mag	Strehl Optimization, 128 actuators, Q1						Strehl Optimization, 128 actuators, Q2					
1	2.74	3.88	3.92	3.95	3.96	3.96	2.32	3.29	3.33	3.36	3.36	3.36
3	2.73	3.87	3.92	3.95	3.95	3.95	2.32	3.28	3.32	3.35	3.35	3.35
5	2.73	3.86	3.91	3.94	3.94	3.95	2.31	3.27	3.31	3.34	3.34	3.34
7	2.71	3.84	3.89	3.92	3.92	3.92	2.28	3.24	3.27	3.30	3.30	3.31
9	2.67	3.78	3.82	3.86	3.86	3.86	2.22	3.14	3.18	3.20	3.21	3.21
10	2.62	3.71	3.76	3.79	3.79	3.79	2.14	3.04	3.07	3.10	3.10	3.10
Mag	Strehl Optimization, 200 actuators, Q1						Strehl Optimization, 200 actuators, Q2					
1	2.94	4.16	4.21	4.25	4.25	4.25	2.74	3.88	3.93	3.96	3.97	3.97
3	2.93	4.15	4.20	4.24	4.24	4.24	2.73	3.87	3.92	3.95	3.96	3.96
5	2.92	4.14	4.19	4.22	4.23	4.23	2.71	3.85	3.89	3.92	3.93	3.93
7	2.89	4.09	4.14	4.18	4.18	4.18	2.66	3.77	3.81	3.85	3.85	3.85
9	2.80	3.97	4.02	4.06	4.06	4.06	2.51	3.56	3.60	3.64	3.64	3.64
10	2.71	3.84	3.88	3.92	3.92	3.92	2.35	3.33	3.37	3.40	3.40	3.40

Note. Tables are given for different AO control systems (Max Speed and Strehl Optimization), 128 and 200 deformable mirror actuators, and Q1 and Q2 observing conditions.

ORCID iDs

Kevin K. Hardegree-Ullman https://orcid.org/0000-0003-3702-0382
Dániel Apai https://orcid.org/0000-0003-3714-5855
Sebastiaan Y. Haffert https://orcid.org/0000-0001-5130-9153
Martin Schlecker https://orcid.org/0000-0001-8355-2107
Markus Kasper https://orcid.org/0000-0002-8425-6606
Jens Kammerer https://orcid.org/0000-0003-2769-0438
Kevin Wagner https://orcid.org/0000-0002-4309-6343

References

Airapetian, V. S., Barnes, R., Cohen, O., et al. 2020, IJAsB, 19, 136
Anglada-Escudé, G., Amado, P. J., Barnes, J., et al. 2016, Natur, 536, 437
Anglada-Escudé, G., Arriagada, P., Vogt, S. S., et al. 2012, ApJL, 751, L16
Anglada-Escudé, G., Tuomi, M., Gerlach, E., et al. 2013, A&A, 556, A126
Apai, D., Banzatti, A., Ballering, N. P., et al. 2019, BAAS, 51, 475
Arney, G. N. 2019, ApJL, 873, L7
Astropy Collaboration, Price-Whelan, A. M., Lim, P. L., et al. 2022, ApJ, 935, 167
Astropy Collaboration, Price-Whelan, A. M., Sipőcz, B. M., et al. 2018, AJ, 156, 123
Astropy Collaboration, Robitaille, T. P., Tollerud, E. J., et al. 2013, A&A, 558, A33
Astudillo-Defru, N., Forveille, T., Bonfils, X., et al. 2017, A&A, 602, A88
Belikov, R., Sirbu, D., Jewell, J. B., Guyon, O., & Stark, C. C. 2021, in Proc. SPIE, 11823
Bergsten, G. J., Pascucci, I., Hardegree-Ullman, K. K., et al. 2023, AJ, 166, 234
Bergsten, G. J., Pascucci, I., Mulders, G. D., Fernandes, R. B., & Koskinen, T. T. 2022, AJ, 164, 190
Bidot, A., Mouillet, D., & Carlotti, A. 2024, A&A, 682, A10
Bixel, A., & Apai, D. 2017, ApJL, 836, L31
Bixel, A., & Apai, D. 2021, AJ, 161, 228
Bonfils, X., Astudillo-Defru, N., Díaz, R., et al. 2018, A&A, 613, A25
Borra, E. F., & Deschatelets, D. 2018, MNRAS, 481, 4841
Brogi, M., & Birkby, J. 2021, in ExoFrontiers; Big Questions in Exoplanetary Science, ed. N. Madhusudhan (Bristol: IOP Publishing), 8
Bugatti, M., Lovis, C., Pepe, F., et al. 2024, in Proc. SPIE, 13096, 2763
Canfield, D. E. 2005, AREPS, 33, 1
Chaloner, W. G. 1989, JGSoc, 146, 171
Charbonneau, D., Brown, T. M., Noyes, R. W., & Gilliland, R. L. 2002, ApJ, 568, 377
Charbonneau, D., Noyes, R. W., Korzennik, S. G., et al. 1999, ApJL, 522, L145
Chauvin, G., Lagrange, A. M., Dumas, C., et al. 2004, A&A, 425, L29
Costa, K. M., Accorsi-Mendonça, D., Moraes, D. J., & Machado, B. H. 2014, Front. Physiol., 5, 104725
Currie, M. H., Meadows, V. S., & Rasmussen, K. C. 2023, PSJ, 4, 83
Czesla, S., Schröter, S., Schneider, C. P., et al., 2019 PyA: Python Astronomy-related Packages, Astrophysics Source Code Library, ascl:1906.010
Damasso, M., Del Sordo, F., Anglada-Escudé, G., et al. 2020, SciA, 6, eaax7467
Damiano, M., & Hu, R. 2022, AJ, 163, 299
Deshler, N., Haffert, S., & Ashok, A. 2024, arXiv:2403.17988
Di Marcantonio, P., Morossi, C., Franchini, M., & Lehmann, H. 2019, AJ, 158, 161
Etiope, G., & Sherwood Lollar, B. 2013, RvGeo, 51, 276

Faria, J. P., Suárez Mascareño, A., Figueira, P., et al. 2022, A&A, 658, A115
Feng, Y. K., Robinson, T. D., Fortney, J. J., et al. 2018, AJ, 155, 200
Fowler, J., Haffert, S. Y., van Kooten, M. A. M., et al. 2023, Proc. SPIE, 12680, 126801U
Fulton, B. J., Petigura, E. A., Howard, A. W., et al. 2017, AJ, 154, 109
Gaia Collaboration, Brown, A. G. A., Vallenari, A., et al. 2021, A&A, 649, A1
Galicher, R., Potier, A., Mazoyer, J., et al. 2024, A&A, 686, A54
Gaudi, B. S., Seager, S., Mennesson, B., et al. 2020, arXiv:2001.06683
Gendron, E., & Léna, P. 1994, A&A, 291, 337
Gilmozzi, R., & Spyromilio, J. 2007, Msngr, 127, 11
Gordon, I., Rothman, L., Hargreaves, R., et al. 2022, JQSRT, 277, 107949
Guyon, O., Pluzhnik, E., Kuchner, M. J., Collins, B., & Ridgway, S. 2006, ApJS, 167, 81
Guzmán-Marmolejo, A., Segura, A., & Escobar-Briones, E. 2013, AsBio, 13, 550
Haffert, S., Males, J., Ahn, K., et al. 2023, A&A, 673, A28
Haffert, S. Y., Males, J. R., Close, L. M., et al. 2024, Proc. SPIE, 13097, 1429
Haqq-Misra, J. D., Domagal-Goldman, S. D., Kasting, P. J., & Kasting, J. F. 2008, AsBio, 8, 1127
Hardegree-Ullman, K. K., Apai, D., Bergsten, G. J., Pascucci, I., & López-Morales, M. 2023, AJ, 165, 267
Hardegree-Ullman, K. K., Zink, J. K., Christiansen, J. L., et al. 2020, ApJS, 247, 28
Harris, C. R., Millman, K. J., van der Walt, S. J., et al. 2020, Natur, 585, 357
Hawker, G. A., & Parry, I. R. 2019, MNRAS, 484, 4855
Herscovici-Schiller, O., Mugnier, L. M., & Sauvage, J.-F. 2017, MNRAS: Letters, 467, L105
Hitchcock, D. R., & Lovelock, J. E. 1967, Icar, 7, 149
Hoeijmakers, H. J., Snellen, I. A. G., & van Terwisga, S. E. 2018, A&A, 610, A47
Hu, R., Ehlmann, B. L., & Seager, S. 2012a, ApJ, 752, 7
Hu, R., & Seager, S. 2014, ApJ, 784, 63
Hu, R., Seager, S., & Bains, W. 2012b, ApJ, 761, 166
Hu, R., Seager, S., & Bains, W. 2013, ApJ, 769, 6
Hunter, J. D. 2007, CSE, 9, 90
Jensen-Clem, R., Hinz, P., von Kooten, M., et al. 2021, Proc. SPIE, 11823, 1182309
Jensen-Clem, R., Hinz, P. M., van Kooten, M. A. M., et al. 2022, Proc. SPIE, 12185, 1218546
Johns, M., McCarthy, P., Raybould, K., et al. 2012, Proc. SPIE, 8444, 84441H
Jolissaint, L. 2010, JEOS, 5, 10055
JWST Transiting Exoplanet Community Early Release Science Team, Ahrer, E.-M., Alderson, L., et al. 2023, Natur, 614, 649
Kasper, M., Beuzit, J.-L., Verinaud, C., et al. 2010, Proc. SPIE, 7735, 77352E
Kasper, M., Cerpa Urra, N., Pathak, P., et al. 2021, Msngr, 182, 38
Kelley, D. S., Karson, J. A., Fruh-Green, G. L., et al. 2005, Sci, 307, 1428
Keppler, M., Benisty, M., Müller, A., et al. 2018, A&A, 617, A44
Konrad, B. S., Alei, E., Quanz, S. P., et al. 2022, A&A, 664, A23
Kopparapu, R. K., Hébrard, E., Belikov, R., et al. 2018, ApJ, 856, 122
Kopparapu, R. K., Ramirez, R. M., SchottelKotte, J., et al. 2014, ApJL, 787, L29
Krissansen-Totton, J., Olson, S., & Catling, D. C. 2018, SciA, 4, eaao5747
Kump, L. R. 2008, Natur, 451, 277
Lagrange, A. M., Gratadour, D., Chauvin, G., et al. 2009, A&A, 493, L21
Landman, R., Snellen, I., Keller, C., et al. 2023, A&A, 675, A157
Lavie, B., Bouchy, F., Lovis, C., et al. 2023, A&A, 673, A69
Leigh, C., Collier Cameron, A., Horne, K., Penny, A., & James, D. 2003, MNRAS, 344, 1271
Lobo, A. H., Shields, A. L., Palubski, I. Z., & Wolf, E. 2023, ApJ, 945, 161
López-Morales, M., Ben-Ami, S., Gonzalez-Abad, G., et al. 2019, AJ, 158, 24
Lovis, C., Snellen, I., Mouillet, D., et al. 2017, A&A, 599, A16
Lustig-Yaeger, J., Meadows, V. S., & Lincowski, A. P. 2019, AJ, 158, 27
Lyons, T. W., Diamond, C. W., Planavsky, N. J., Reinhard, C. T., & Li, C. 2021, AsBio, 21, 906
Lyons, T. W., Reinhard, C. T., & Planavsky, N. J. 2014, Natur, 506, 307
Macintosh, B., Graham, J. R., Barman, T., et al. 2015, Sci, 350, 64
Madec, P.-Y., Ströbele, S., Kasper, M., et al. 2022, Proc. SPIE, 12185, 1218525
Madhusudhan, N., Sarkar, S., Constantinou, S., et al. 2023, ApJL, 956, L13
Males, J. R., Close, L. M., Haffert, S. Y., et al. 2022, Proc. SPIE, 12185, 121854J
Males, J. R., Close, L. M., Haffert, S. Y., et al. 2024, Proc. SPIE, 13096, 130960Y
Males, J. R., Fitzgerald, M. P., Belikov, R., & Guyon, O. 2021, PASP, 133, 104504
Males, J. R., & Guyon, O. 2018, JATIS, 4, 019001
Mamajek, E., & Stapelfeldt, K. 2024, arXiv:2402.12414
Marois, C., Macintosh, B., Barman, T., et al. 2008, Sci, 322, 1348
Martins, J. H. C., Santos, N. C., Figueira, P., et al. 2015, A&A, 576, A134
McKinney, W. 2010, in Proc. 9th Python in Science Conf., ed. S. van der Walt & J. Millman (Austin, TX: SciPy), 56
Meadows, V. S. 2017, AsBio, 17, 1022
Meadows, V. S., Arney, G. N., Schwieterman, E. W., et al. 2018a, AsBio, 18, 133
Meadows, V. S., Reinhard, C. T., Arney, G. N., et al. 2018b, AsBio, 18, 630
Moran, S. E., Stevenson, K. B., Sing, D. K., et al. 2023, ApJL, 948, L11
Morris, B. M., Tollerud, E., Sipőcz, B., et al. 2018, AJ, 155, 128
NASEM 2021, Pathways to Discovery in Astronomy and Astrophysics for the 2020s (Washington DC: The National Academies Press)
Nelson, J., & Sanders, G. H. 2008, Proc. SPIE, 7012, 70121A
pandas Development Team 2020, pandas-dev/pandas: Pandas, Zenodo, doi:10.5281/zenodo.3509134
Pidhorodetska, D., Fauchez, T. J., Villanueva, G. L., Domagal-Goldman, S. D., & Kopparapu, R. K. 2020, ApJL, 898, L33
Potier, A., Mazoyer, J., Wahhaj, Z., et al. 2022, A&A, 665, A136
Prieto, G., Thomas-Osip, J. E., Phillips, M. M., McCarthy, P., & Johns, M. 2010, Proc. SPIE, 7733, 77334O
Quanz, S. P., Ottiger, M., Fontanet, E., et al. 2022, A&A, 664, A21
Rains, A. D., Ireland, M. J., Jovanovic, N., et al. 2016, Proc. SPIE, 9908, 990876
Rauer, H., Aerts, C., Cabrera, J. & PLATO Team 2016, AN, 337, 961
Robinson, T. D., & Salvador, A. 2023, PSJ, 4, 10
Rodler, F., & López-Morales, M. 2014, ApJ, 781, 54
Sagan, C., Thompson, W. R., Carlson, R., Gurnett, D., & Hord, C. 1993, Natur, 365, 715
Sanders, G. H. 2013, JApA, 34, 81
Sarazin, M., Le Louarn, M., Ascenso, J., Lombardi, G., & Navarrete, J. 2013, in Proc. Third AO4ELT Conf., ed. S. Esposito & L. Fini (Firenze: AO4ELT)
Sauvage, J.-F., Mugnier, L. M., Rousset, G., & Fusco, T. 2010, JOSA A, 27, A157
Scandariato, G., Borsa, F., Sicilia, D., et al. 2021, A&A, 646, A159
Schlecker, M., Apai, D., Lichtenberg, T., et al. 2024, PSJ, 5, 3
Segura, A., Kasting, J. F., Meadows, V., et al. 2005, AsBio, 5, 706
Serindag, D. B., & Snellen, I. A. G. 2019, ApJL, 871, L7
Sessions, A. L., Doughty, D. M., Welander, P. V., Summons, R. E., & Newman, D. K. 2009, 19, R567
Shields, A. L., Ballard, S., & Johnson, J. A. 2016, PhR, 663, 1
Shields, A. L., Meadows, V. S., Bitz, C. M., et al. 2013, AsBio, 13, 715
Sing, D. K., Fortney, J. J., Nikolov, N., et al. 2016, Natur, 529, 59
Snellen, I., de Kok, R., Birkby, J. L., et al. 2015, A&A, 576, A59
Snellen, I. A. G., Albrecht, S., de Mooij, E. J. W., & Le Poole, R. S. 2008, A&A, 487, 357
Snellen, I. A. G., de Kok, R. J., de Mooij, E. J. W., & Albrecht, S. 2010, Natur, 465, 1049
Snellen, I. A. G., de Kok, R. J., le Poole, R., Brogi, M., & Birkby, J. 2013, ApJ, 764, 182
Sparks, W. B., & Ford, H. C. 2002, ApJ, 578, 543
Speagle, J. S. 2020, MNRAS, 493, 3132
Spring, E. F., Birkby, J. L., Pino, L., et al. 2022, A&A, 659, A121
Stevenson, K. B., Bean, J. L., Seifahrt, A., et al. 2014, AJ, 147, 161
Susemiehl, N., Mandell, A. M., Villanueva, G. L., et al. 2023, AJ, 166, 86
Thauer, R. K., & Shima, S. 2008, NYASA, 1125, 158
The LUVOIR Team 2019, arXiv:1912.06219
Thomas-Osip, J. E., McCarthy, P., Prieto, G., Phillips, M. M., & Johns, M. 2010, Proc. SPIE, 7733, 77331L
Tsai, S.-M., Innes, H., Wogan, N. F., & Schwieterman, E. W. 2024, ApJL, 966, L24
Turbet, M., Leconte, J., Selsis, F., et al. 2016, A&A, 596, A112
Van Gorkom, K., Males, J. R., Close, L. M., et al. 2021, JATIS, 7, 039001
Vaughan, S. R., Birkby, J. L., Thatte, N., et al. 2024, MNRAS, 528, 3509
Walter, A. B., Fruitwala, N., Steiger, S., et al. 2020, PASP, 132, 125005
Wang, J., Mawet, D., Ruane, G., Hu, R., & Benneke, B. 2017, AJ, 153, 183
Wogan, N. F., Batalha, N. E., Zahnle, K. J., et al. 2024, ApJL, 963, L7
Wordsworth, R., & Pierrehumbert, R. 2014, ApJL, 785, L20
Wright, D. J., Wittenmyer, R. A., Tinney, C. G., Bentley, J. S., & Zhao, J. 2016, ApJL, 817, L20
Wunderlich, F., Godolt, M., Grenfell, J. L., et al. 2019, A&A, 624, A49
Zahnle, K., Freedman, R. S., & Catling, D. C. 2011, Icar, 212, 493
Zahnle, K. J., & Catling, D. C. 2017, ApJ, 843, 122
Zhang, H., Wang, J., & Plummer, M. K. 2024, AJ, 167, 37
Zhang, Z., Zhou, Y., Rackham, B. V., & Apai, D. 2018, AJ, 156, 178